



Cyprus  
University of  
Technology



杭州电子科技大学  
HANGZHOU DIANZI UNIVERSITY

**Master's Thesis**

**Hybrid neural network based multi-objective optimal design  
of hybrid pin-fin microchannel heatsink for integrated  
microsystems**

**Cheng-Yi, Feng**

**Limassol, Month and year of thesis submission**



MSc in Electronics Science  
and Technology

CYPRUS UNIVERSITY OF TECHNOLOGY  
FACULTY OF ENGINEERING AND TECHNOLOGY  
DEPARTMENT OF ELECTRICAL ENGINEERING AND COMPUTER  
ENGINEERING AND INFORMATICS

Master's Thesis

Hybrid neural network based multi-objective optimal design of  
hybrid pin-fin microchannel heatsink for integrated microsystems

Cheng-Yi, Feng

Paul Christodoulides

Department of Electrical Engineering, Computer Engineering and Informatics,  
University of Technology, Cyprus

Limassol, December 2024

# **Approval Form**

Master's Thesis

## **Hybrid neural network based multi-objective optimal design of hybrid pin-fin microchannel heatsink for integrated microsystems**

Presented by

Cheng-Yi, Feng

Supervisor: Paul Christodoulides

Member of the committee: [Name Surname and position]

Member of the committee: [Name Surname and position]

Cyprus University of Technology

Limassol, May 2025

## **Copyrights**

Copyright© 2025 Chengyi, Feng

All rights reserved.

The approval of the thesis by the Department of Electrical Engineering and Computer Engineering and Informatics does not necessarily imply the approval by the Department of the writer's views.

## **Acknowledgments**

The success of this research is mainly due to the guidance of Professor Paul Christodoulides of Cyprus University of Technology and Professor Wen-Sheng Zhao of Hangzhou Dianzi University. Their profound knowledge not only guided this research through the critical conceptual stage, but also enhanced the academic rigor of this research through their insightful guidance. At the same time, I sincerely thank Dr. Lazaros Aresti for his technical guidance during the process. I pay my deepest respect and sincere gratitude to these respected scholars.

In addition, special thanks to faculties and staffs of the Department of Electrical Engineering, Computer Engineering and Informatics for their support. They generously shared their professional methods and jointly built a comfortable research environment, which fully reflects their collective wisdom.

Finally, and very importantly, I would like to thank my family, whose unwavering encouragement supported my continuous pursuit of academic pursuits and their silent dedication constituted the invisible cornerstone of this achievement.

## ABSTRACT

With the rapid advancement of 2.5D/3D heterogeneous integrated microsystems, the performance and fast intelligent design for thermal management are unprecedentedly required to address the electrical and mechanical reliability issues caused by thermal runaway.

In this work, a hybrid neural network, featuring a small dataset requirement, is developed to accelerate the design of the hybrid pin-fin microchannel heatsink. Assisted by the trained machine learning surrogate model and the non-dominated sorting genetic algorithm, a powerful heatsink characterizing power-adaptive cooling capacity is designed. In this study, firstly, a hybrid pin-fin microchannel heatsink is modeled. Then the grid test and simulation validity are carried out. The critical structural parameters correlated with the heat transfer and hydraulic performance are analyzed and identified through numerical simulation. A hybrid neural network serving as a surrogate model, is then developed to map the relationship between key structural parameters and the targeted performance indexes.

The hybrid neural network achieves a prediction accuracy of at least 94.33% and outperforms traditional networks, including DNN and CNN, in RMSE, MAE, and RE. It improves by 93.4%, 89.5%, and 87.8% over DNN, and by 91.7%, 93.0%, and 91.9% over CNN. The non-dominated sorting genetic algorithm is performed to explore the Pareto front where the intelligent design of power-adaptive pin-fin layout under uneven thermal profile is achieved. The performance indexes of the optimized heatsink are validated with that from the computational fluid dynamics. Compared with the original structure, it is found that enhancements of 5.58%, 10.76% and 45.73% are achieved in the maximum temperature of high-power heat source, low-power heat source and the pressure drop of microchannel.

**Keywords:** Keywords: Microchannel Heatsink, Integrated microsystems, Machine learning, Genetic algorithm, Semi-supervised learning

# Table of Contents

ABSTRACT.....	v
LIST OF TABLES.....	vii
LIST OF FIGURES.....	viii
LIST OF ABBREVIATIONS.....	x
1 Introduction.....	1
2 Literature review.....	4
3 Research Methodology.....	12
3.1 Physical model.....	12
3.2 Governing equations and boundary conditions.....	14
3.3 Grid independence analysis.....	16
3.4 Validation of numerical results.....	18
3.5 Hybrid neural network.....	18
3.6 Labelled dataset construction.....	20
3.7 Multi-objective non-dominated sorting genetic algorithm optimization.....	22
4 Results.....	24
4.1 Comparison of different design paraments.....	24
4.1.1 Lateral spacing between pin-fins.....	24
4.1.2 Longitudinal spacing between pin-fins.....	27
4.1.3 Radius of the pin-fin.....	29
4.1.4 Height of the pin-fin.....	31
4.1.5 Width of the microchannel.....	33
4.2 Hybrid NN Method.....	34
4.3 Optimization with NSGA-II.....	36
5 Conclusion.....	39
BIBLIOGRAPHY.....	41

## **LIST OF TABLES**

Table 1. Thermophysical properties of materials. ....	13
Table 2: Comparison of predictive accuracy of the conventional CNN, DNN and the developed HNN .....	35
Table 3. Comparison of temperature and pressure drop results between the initial and optimal HPFMCHS.....	38
Table 4. Optimal HPFMCH structure parameters .....	39

## LIST OF FIGURES

Figure. 1. Schematics of (a) the overall view, (b) cross section view, (c) top view and (d) bottom view of a microchannel unit. ....	13
Figure. 2. Configuration of boundary conditions on the proposed HPFMCHS model. (a) top view and (b) bottom view .....	15
Figure. 3. Grid sensitivity tests of (a) the peak temperature and (b) pressure drop of the heatsink versus the number of mesh nodes.....	17
Figure. 4. Computational grid of proposed HPFMCHS. ....	17
Figure. 5. Comparative results of (a) temperature from CFD simulation and experiment conducted by Wei et al. [117] and (b) pressure drop from simulation and experiment conducted by Qu and Mu-dawar [118]. ....	18
Figure. 6. (a) Flowchart of HNN and the structures of (b) CNN and (c) DNN.....	20
Figure. 7. (a) The variables to be optimized and (b) the flowchart of the legal layout generation of pin-fin array. ....	22
Figure. 8. Flowchart of the NSGA-II.....	24
Figure. 9. Field distributions of (a) temperature, (b) pressure, and (c) velocity when $Re = 200$ for different lateral spacing of pin-fins. ....	26
Figure. 10. Effects of lateral spacing of pin-fins on (a) peak temperature of chips and (b) the pressure drop. ....	27
Figure. 11. Field distributions of (a) temperature, (b) pressure and (c) velocity when $Re = 200$ for different pin-fin longitudinal spacing. ....	28
Figure. 12. Effects of longitudinal spacing on (a) peak temperature of chips and (b) pressure drop.....	29
Figure. 13. Field distributions of (a) temperature, (b) pressure and (c) velocity when $Re = 200$ for different pin-fin radius. ....	30
Figure. 14. Effect of pin-fin radius on temperature (a) and (b) pressure drop.....	30
Figure. 15. Field distributions of (a) temperature, (b) pressure and (c) velocity when $Re = 200$ for different pin-fin height. ....	31

Figure. 16. Effect of pin-fin height on temperature (a) and (b) pressure drop. ....	32
Figure. 17. Field distributions of (a) temperature, (b) pressure and (c) velocity at when $Re = 200$ for different channel width. ....	33
Figure. 18. Effect of channel width on temperature (a) and (b) pressure drop.....	34
Figure. 19. Predictive error of HNN between predicted and actual values of (a) the maximal temperature of the HPHS, (b) the maximal temperature of LPHS and (c) the pressure drop in the microchannel. ....	36
Figure. 20. Variations in temperature and pressure drop of (a) the first generation, (b) the fifth generation, (c) the fifteenth generation, (d) the one hundred-generation and (e) optimal decision point of Pareto front in the final generation population. ....	37
Figure. 21. Optimal structure of HPFMCHS.....	39

## LIST OF ABBREVIATIONS

$A$	Area, m <sup>2</sup>
$A_{ch}$	Cross-section area of the microchannel, m <sup>2</sup>
$x$	Lateral spacing between pin-fins, mm
$y$	Longitudinal spacing between pin-fins, mm
$dx$	Lateral spacing change between pin-fins, mm
$dy$	Longitudinal spacing change between pin-fins, mm
$r$	Pin-fin radius, mm
$h$	Pin-fin height, mm
$W_{ch}$	Lateral width of the channel, mm
$W_{tot}$	Width of a half microchannel unit, mm
$W_{ao}$	Outer length of the region of pin-fins array, mm
$W_{ai}$	Inner length of the region of pin-fins array, mm
$L$	Overall length of the heatsink, mm
$L_{yh}$	Euclidean distance
$X$	Input of neural network
$Y$	Output of neural network
$H_{tot}$	Inner height of microchannel, mm
$H_{ch}$	Outer height of microchannel, mm
$\mu$	Dynamic viscosity, kg · m <sup>-1</sup> · s <sup>-1</sup>
$\rho$	Density, kg · m <sup>-3</sup>
$T$	Temperature, K
$T_1$	Maximal temperature of HPHS, K
$T_2$	Maximal temperature of LPHS, K

$\Delta p$	Microchannel pressure drop, kPa
$q$	Heat flux, W/m <sup>2</sup>
$Q$	Flow rate, ml/min
$k$	Thermal conductivity, W · m <sup>-1</sup> · K <sup>-1</sup>
$c_p$	Specific heat capacity, J/(kg · K)
$u$	Velocity, m/s
$w$	Width, mm
<b>Subscripts</b>	
$f$	Fluid
$in$	Inlet
$s$	Solid
$w$	Wall
<b>Abbreviations</b>	
MCHS	Microchannel heatsink
HPFMCHS	Hybrid pin-fin microchannel heatsink
GA	Genetic algorithm
NSGA-II	Non-dominated sorting genetic algorithm
CFD	Computational fluid dynamics
HPS	High-power heat source
LPHS	Low-power heat source
ANN	Artificial neural network
CNN	Convolutional neural network
DNN	Deep neural networks
HNN	Hybrid neural network

RMSE	Root-mean-square error
MAE	Mean absolute error
RE	Relative error

# 1 Introduction

As transistor sizes in integrated circuits (ICs) continue to shrink, Moore's Law is approaching its physical limits [1]. The first microprocessor developed by Intel in 1971 had only 2,300 transistors. According to Gordon Moore's projected roadmap, this number has now risen to 5.4 billion [2]. Increasing design complexity and dynamic power consumption in single-core processors have driven microprocessor architecture towards multi-core technology [3-4]. The heat flux generated in the core is significantly higher than in the remaining areas of the microprocessor, with these high heat flux areas referred to as hotspots. The substantial temperature gradient resulting from the difference in heat flux between the core and background regions can significantly reduce microprocessor lifespan [5-6]. However, multi-core technology alone is insufficient; the number of transistors, constrained by area and process limits, has nearly reached its maximum. To meet the growing computational demands of the era of artificial intelligence (AI) and large-scale data processing, three-dimensional stacked integrated circuits (3D-ICs) have emerged as a key technological innovation [7]. By vertically stacking multiple silicon chips, 3D-ICs integrate more transistors within limited space, thereby enhancing processing power. Although 3D-IC technology holds significant potential in overcoming the physical limitations of Moore's Law, harmful thermal issues, such as electrical failures and mechanical fatigue caused by high heat flux density, are becoming bottlenecks that hinder further improvements in overall system performance [8-10]. Localized overheating can lead to performance degradation or even device failure, with approximately 55% of electronic device failures attributed to inadequate heat dissipation [11-12].

However, modern air cooling technologies have reached their limit [13] and are insufficient to meet the high thermal dissipation demands of today's ultra-thin electronic devices. How to effectively manage the heat generated by these devices has become a key challenge in realizing efficient electronic systems. Various new electronic cooling technologies have emerged, such as liquid metal cooling, microchannel cooling, impingement jet cooling, and immersion liquid cooling [14-17]. Among them, microchannel heat sink (MCHS) has attracted widespread attention due to their high integration potential. Due to its small size and short heat transfer distance, this technology

has become a research hotspot in recent years. Therefore, this paper focuses on the microchannel heat sink designed for 3D-ICs.

A large number of research results show that the heat transfer characteristics of single-phase forced convection in microchannels are closely related to the geometric parameters of the channel. The hydraulic diameter and the depth-to-width ratio of the channel are used as parameters to measure the microchannel structure [18-19]. Considering that parallel and regular structures are relatively easy to manufacture, rectangular MCHS with high aspect ratios are often used in related studies. However, simply changing the shape of the microchannel is not enough. Due to the rapid increase in heat accumulation in microprocessors, research has gradually turned to complex microchannel internal structures [20]. Microfluids are important heat transfer media in microchannels. The way they flow affects the overall thermal performance of the heat sink. Ribs and pin-fins are widely used to enhance heat transfer in microchannels due to their high thermal conductivity and obvious effect on fluid disturbance [21]. Common rib and pin-fin shapes include circular, elliptical, rectangular, diamond, and triangular. In addition to changing the shapes of pin-fins and ribs, changing their arrangement such as rectangular oblique ribs, sidewall staggered ribs, staggered trapezoidal ribs and V-shaped ribs can also affect the performance of the heat sink to a certain extent. The effect of these structures on the performance shows that the hybrid structure heat sink has better heat dissipation efficiency than the traditional straight microchannel heat sink. Excellent MCHS should dissipate more heat at a lower pumping power. Thermal resistance, temperature distribution and pressure drop are all important criteria for evaluating the overall performance of MCHS [22]. This study proposes a modular microchannel heat dissipation design method, by extracting and optimizing the flow channel aspect ratio, hydraulic diameter, channel shape and enhanced structure of the microchannel, and finally evaluating the overall heat dissipation performance of the heat sink with thermal resistance, pressure drop or improved temperature uniformity as evaluation indicators.

However, chips with different heat distributions require targeted design of different optimization situations. It is far from enough to design the heat sink based on experimental experience. In order to achieve rapid optimization of the heat sink combination, an efficient optimization algorithm needs to be selected. As a classic global optimization algorithm, the genetic algorithm (GA) has strong global optimization

capabilities, and the non-dominated sorting genetic algorithm (NSGA-II) is further improved on this basis [23]. NSGA-II significantly improves the optimization efficiency by hierarchically ranking individuals between dominated and non-dominated individuals and giving priority to retaining non-dominated solutions in the selection operation. Therefore, NSGA-II was selected as the main optimization algorithm for this study. Before applying the optimization algorithm, it is necessary to clarify the numerical expression of the optimization objective.

Since the correlation between optimization objectives and design variables is often complex, constructing high-quality expressions relies on large data sets [24]. However, the acquisition of these data often requires the use of computational fluid dynamics (CFD) or experimental measurements, which is time-consuming and computationally expensive. Although NSGA-II has efficient optimization capabilities, the traditional CFD-optimization coupling method still has low overall efficiency due to the high cost of CFD calculations. In order to overcome this bottleneck, this paper proposes a surrogate model method based on machine learning (ML) [25], which is designed to replace the CFD simulation output of key performance parameters (such as temperature, pressure drop, etc.), thereby accelerating the optimization process of NSGA-II. However, existing research shows that building accurate ML surrogate models often requires large-scale data sets, and the high computational cost of finite element simulation makes obtaining large data sets extremely challenging. Therefore, how to use small data sets to build high-precision surrogate models has become one of the key issues in this research. To address this problem, this paper designs a semi-supervised hybrid neural network (HNN) to fully mine the potential information of small data sets to train an agent model with high prediction accuracy and strong generalization ability [26]. By introducing this surrogate model to replace CFD, the need for CFD iterative calculations can be greatly reduced during the optimization process. Compared with the traditional CFD and GA coupling optimization method, the combined method based on ML agent model and NSGA-II significantly improves the optimization efficiency and provides an innovative path for efficient optimization of complex multi-physics problems.

In summary, the purpose of this study is to optimize the structure and layout of the chip heat sink to achieve maximum heat dissipation efficiency. The method to achieve this optimization is to continuously iterate and select the best parameter combination through

optimization algorithms such as NSGA-II. In order to speed up the iteration and avoid the tedious calculation process of CFD, HNN is used as a proxy model to replace CFD. The paper is divided into three chapters. The first chapter will comprehensively explain the literature related to this study in recent years, compare the advantages and disadvantages of the methods, and explain what content this study refers to in previous studies and how it has been improved compared with previous studies. The second chapter will explain the heat sink structure model proposed in this study, give the simulation formula and heat sink evaluation indicators, and verify the validity of the computational fluid dynamics (CFD) results and calculate the grid convergence. And the HNN and optimization algorithm used in the study will also be introduced in detail. The third chapter will perform CFD simulation on the heat sink, compare and analyze the various design parameters, and finally extract the parameters that have a greater impact on the comprehensive thermal performance of the heat sink. The structural data composed of these parameters are used for batch simulation in the software. After obtaining the complete data set, the HNN is trained. After obtaining the proxy model, its accuracy is tested. Finally, the proxy model is used to accelerate the optimization algorithm to find the optimal heatsink structure and layout. The optimal heat sink is simulated by CFD, and finally the evaluation and comparison of the corresponding parameters are given.

## **2 Literature review**

In 1981, Tuckerman et al. first proposed the concept of microchannel heat sinks (MCHS), highlighting their significant advantages over traditional heat dissipation methods [27]. The fundamental design principle of MCHS involves integrating microscale fluid channels within a compact chip or substrate, allowing the rapid removal of heat generated by the chip via the flow of coolant through these channels. By incorporating microchannels directly into the packaging, heat can be dissipated directly from the heat source through the microchannel heat sink. Compared to other cooling methods, MCHS offers superior thermal performance and a smaller footprint, facilitating integration into micro systems. Additionally, the high surface area-to-volume ratio of microchannels allows efficient heat transfer along the shortest path, significantly enhancing heat dissipation. MCHS demonstrates a higher heat transfer coefficient and can reduce coolant consumption compared to conventional air or liquid cooling methods, making it promising for applications in modern high-power-density electronic devices [28-31]. In

recent years, many studies have focused on how to further improve the heat dissipation performance of MCHS, especially in the face of the continuous shrinking of electronic devices and the continuous increase in power density. Erp et al. [32] co-designed a microfluidic cooler and electronic devices on the same substrate, resulting in a monolithic integrated cooling structure with manifold microchannels. The study found that a heat flux of more than  $1.7 \text{ kW/cm}^2$  could be dissipated with a pump power of  $0.57 \text{ W/cm}^2$ . However, due to the presence of a hydrothermal boundary layer in the heat sink with parallel straight microchannels, the cooling potential was not fully utilized. This view has been confirmed by many previous studies [33].

However, previous scholars often used experiments to verify the heat dissipation capacity of microchannels, but the complex structure and process requirements of microchannels increased the difficulty of experimental research. Therefore, numerical research methods can become an effective tool for dealing with complex problems. Feng et al. [34] applied CFD to simulate the laminar flow and heat transfer characteristics of rectangular nested coil microchannels and used the finite volume method to solve the control equations. Their research results showed that the coils in the microchannels can enhance fluid disturbance and improve temperature distribution. The maximum deviation between the experimental data and the numerical calculation results was 14.2%. Liu et al. [35] used the CFD method to study an annular inclined microchannel with multiple staggered inlets and outlets. The simulation results showed that the staggered arrangement had a more uniform temperature distribution than the sequential arrangement. Yang and Cao [36] proposed a new hybrid microchannel heat sink by changing the inlet length, secondary channel width and Reynolds number (Re) of the microchannel heat sink. They said that compared with the traditional MCHS, the new MCHS can effectively reduce pressure loss due to its flow characteristics. Lu and Zhai [37] applied computational fluid dynamics to study the heat transfer and flow characteristics of MCHS combined with dimples and vortex generators. The results show that the combination of vortex concavities and vortex generators can improve heat transfer performance and reduce pressure loss. Ling et al. [38] conducted a combined CFD simulation and experimental study to study the heat transfer and flow characteristics of a new type of staggered microchannel, and used conjugate heat transfer numerical simulation to optimize the structure. The analysis of experimental and simulation results showed that the Nusselt number of the staggered

microchannel was 65.4% higher than that of the parallel microchannel, and the surface temperature distribution was more uniform. In their study, the deviation between the experimental data and the simulation results was less than 18%. Ali et al. [39] proposed a four-quadrant microchannel heat sink (4 QMCHS) and established a three-dimensional conjugate heat transfer model to study its temperature distribution. The results show that the inlet and outlet directions have a great influence on the non-uniformity of the temperature distribution, and the temperature distribution of the heat sink using the counterflow method is relatively uniform. Peng et al. [40] used 3D CFD to simulate the flow and heat transfer process in a multi-jet microchannel (MJMC) heat sink, where the coolant flows through alternating inlet and outlet jets in a direction perpendicular to the heating surface. Compared with traditional microchannels, microjet microchannels combine the advantages of impinging jets and microchannel inlet effects. Lin et al. [41] proposed a new MCHS with variable wavelength and variable amplitude along the flow direction. They found that this variation can effectively mix the coolant and enhance heat transfer. Hasis et al. [42] conducted a CFD study to simulate laminar flow and heat transfer in a twisted sinusoidal microchannel. The results showed that the heat transfer performance of the twisted corrugated channel was better than that of the sinusoidal corrugated channel. Lei and Chen [43] numerically studied the heat transfer and pressure drop characteristics of supercritical carbon dioxide in a horizontal corrugated microchannel (WMCCT) with consistent crests and troughs and a corrugated microchannel (WMOCT) with opposite crests and troughs. The results showed that the heat transfer coefficient and pressure drop of WMCCT and WMOCT increased with increasing amplitude and decreased with decreasing wavelength. Sreehari and Sharma [44] combined computational fluid dynamics methods with experimental work to analyze the overall performance of three different rectangular cross-section serpentine microchannels at different Reynolds numbers and heat fluxes. They reported that the U-shaped serpentine microchannel showed the best thermal performance compared to the other two serpentine microchannels. The experimental data were compared with the simulation results, and the pressure drop deviation was 10-11% and the average base temperature deviation was 1-3%. It can be seen that simulation through CFD has extremely high accuracy and can provide a good research method for MCHS numerical simulation.

An 3D-ICs system usually includes components of different processes, resulting in different power and heat generation of each part. Conventional cooling solutions with uniform heat transfer coefficient (HTC) distribution lead to supercooling of background areas and supercooling of hotspot areas, resulting in intensive energy consumption and significant temperature non-uniformity. Therefore, to deal with this situation, traditional microchannel heat sinks are obviously not suitable, and there is an urgent need to create non-uniform HTC distribution to adapt to the non-uniformity of heat flux on the chip heat source area. Hybrid pin-fin microchannel heat sink (HPFMCHS) is an innovative design create non-uniform HTC. HPFMCHS is selectively designed according to the different locations of multiple heat sources. In order to enhance the local convection effect between the coolant and the channel sidewalls to adapt to the situation where high-power and low-power heat sources exist simultaneously, Ansari et al. [45] proposed a HPFMCHS that uses rectangular microchannels in low heat flux areas and a series of cylindrical pin fins in high heat flux areas. Thanks to the enlarged effective heat transfer area and the stronger eddy effect brought by the pin fin array, compared with the traditional smooth microchannel heat sink, only 11.7% of additional pump power is required to reduce the hot spot temperature rise by 30.6% under the condition of Reynolds number of 200. Tang et al. [46] designed a new type of manifold ultra-thin micro pin fin heat sink (MUMPFHS) and studied the thermal, energy and exergy performance of the system in cooling  $10\times 10\text{mm}^2$  high-concentration photovoltaic (HCPV) cells through numerical simulation. Under the conditions of an inlet flow rate of 3 kg/h and a coolant temperature of  $25^\circ\text{C}$ , the temperature of the solar cell was reduced to  $51^\circ\text{C}$ , and the temperature non-uniformity was only  $3.4^\circ\text{C}$ . Compared with the designs of jet cooling, mixed jet/microchannel cooling, and stepped variable width microchannel, the new design showed higher temperature uniformity and cooling performance at 1000 times the solar concentration. In addition, the significant modularity of HPFMCHS facilitates the independent analysis and design of the microchannel section and the pin fin area, so that the structural parts can be optimized in a targeted manner to improve the heat dissipation performance. Many scholars have studied the effects of the shape and layout of the pin fins on the heat dissipation capacity, and proposed some suitable pin fin structures and layouts [47-60]. Research have shown that factors such as the shape, size, and arrangement of the microchannel will directly affect the flow characteristics and heat transfer efficiency of the fluid [47]. To increase convective heat transfer area, slanted fan shapes [48], droplet

shapes [49], trapezoidal [50], and triangular cavities [51-52] are commonly added within microchannels. However, cavity structures have limitations in improving hydrothermal performance, as fluid in these cavities can form stagnation zones, hindering flow and raising local temperatures, ultimately affecting overall heat transfer [52]. Adding straight ribs of various shapes within microchannels is another approach to enhance heat transfer. Inspired by studies on solar air heaters with semi-circular [53], triangular [54-55], and compound ribs [56], researchers have added different rib structures—triangular [57], elliptical [58], cylindrical sidewalls [59], and diamond-shaped [60] ribs to microchannel heat sinks. Despite improved heat transfer performance from rib-only designs, increased flow resistance often deteriorates flow characteristics [52]. Thus, studies have observed that neither ribs nor cavities alone can simultaneously optimize heat transfer and flow performance. Consequently, researchers are now exploring the combined use of these approaches to analyze the thermal performance of water-based systems.

Xia et al. [61] investigated a novel heat sink featuring circular grooves and semi-circular sidewall ribs in microchannels, optimizing parameters such as relative groove height, rib height, and rib width. Datta et al. [62] combined four different rib shapes (rectangular, rear triangular, front triangular, and diamond) with trapezoidal cavities, examining how variations in cavity relative width and length, as well as rib relative width and spacing, influenced thermal performance. Yan et al. [63] proposed a pin-fin array with a graded distribution and narrow-step structure to enhance overall thermal performance by reducing pressure drop. This design slightly raised the overall heat sink temperature but significantly reduced pressure drop while maintaining uniform surface temperature distribution. Lawson et al. [64] demonstrated that the transverse and longitudinal pitch of pin-fins notably affected the thermal-hydraulic performance of the heat sink, with transverse pitch being more influential. Chiu et al. [65] observed that for small-diameter circular pin-fins, heat transfer performance declined, and porosity values above 0.7 had negligible impact on thermo-hydraulic behavior. Feng et al. [66] highlighted the effectiveness of interrupted microchannel heat sinks, which integrated microchambers and circular pin-fins. Their findings indicated that larger pin-fin diameters in individual microchambers enhanced thermal management, though with some compromise in fluid dynamics. Additionally, they noted a positive but limited effect of longitudinal spacing on thermal performance. In an analytical study, Khan et al. [67] reported that inline fin

arrangements exhibited lower friction coefficients but higher thermal resistance than staggered arrangements. Mohammadi et al. [68] studied staggered pin-fin configurations, attributing improved thermal performance to intensified boundary layer disruption behind the fins. John et al. [69] simulated microchannel flow through circular and square pin-fins, concluding that smaller hydraulic diameters and higher aspect ratios of pin-fins yielded better thermal-hydraulic performance. Sertkaya et al. [70] conducted experiments on pin-fin and plate heat sinks, identifying a threshold in pin-fin count that impacted heat transfer efficiency. Pin-fin geometry is another critical aspect of heat sink thermal-hydraulic performance. Boundary layer disruption, associated with backflow, was found to degrade fluid dynamics but enhance heat transfer. In this regard, sharp-edged pin-fins, due to strong downstream flow separation and vortices, offered better thermal performance, whereas streamlined pin-fins were advantageous for fluid dynamics. Vilarrubi et al. [71] compared pin-fin and elongated rectangular fin performance in microchannels, finding that pin-fins maintained lower peak temperatures at chip hotspots. Huang et al. [72] analyzed conjugate heat transfer in optimized pin-fin shapes, achieving a 34% enhancement in heat transfer performance. Ahmadian et al. [73] performed parametric simulations on thermal-hydraulic performance, demonstrating that conical circular pin-fins improved overall heat sink performance by 17%. In conclusion, parameter variations substantially influence heat sink performance.

As integrated microsystems grow in complexity, precise heat sink design becomes crucial. Relying solely on empirical methods and experimental trials to design microchannel heat sink (MCHS) structures is both time-intensive and unlikely to yield optimal solutions. Therefore, efficient methods for rapid heat sink structural optimization are essential. Genetic algorithms (GA), a widely used optimization technique, are frequently applied for multi-objective MCHS optimization. By establishing relationships between variables and objectives based on an initial set of numerical or analytical results, GA enables comprehensive multi-objective analysis [74-76]. GA emulates natural selection and evolutionary processes, enabling efficient exploration of optimal solutions within complex design spaces. Building on the classic GA, the Non-Dominated Sorting Genetic Algorithm (NSGA) introduces the concept of crowding distance to search for the optimal Pareto frontier formed by non-dominated individuals [77]. Due to its effective optimization in trade-off designs with numerous variables, NSGA is widely applied in

multi-objective black-box problem optimization [78]. Yildizeli and Cadirci [79] applied NSGA-II to optimize the thermal and fluid-dynamic performance of rectangular MCHSs. By iteratively adjusting channel width, height, and inlet Reynolds number, they achieved MCHS designs with reduced pressure drop and temperature. Similarly, Foli et al. [80] employed computational fluid dynamics (CFD) simulations to optimize the aspect ratio of rectangular channels in micro heat exchangers, refining parameters using NSGA-II. This resulted in a 70% reduction in pressure drop on the thermal fluid side and a 73% improvement in heat transfer efficiency. Leng et al. [81] used a simplified NSGA to minimize thermal resistance in a dual-layer MCHS under varying thermal and fluid-dynamic constraints. Results demonstrated that smaller microchannel cross-sectional areas enhance heat transfer, albeit with increased pumping power. Wang et al. [82] integrated a CFD solver with NSGA-II to optimize the design of a semi-porous ribbed dual-layer heat sink, simultaneously minimizing key performance indicators such as channel count, rectangular channel aspect ratio, channel spacing ratio, and flow characteristics, leading to optimized pump power and overall thermal resistance. Likewise, NSGA-II combined with response surface methodology enabled optimization of a hybrid MCHS design with embedded secondary channels and manifolds, resulting in an 18.8% reduction in thermal resistance at equivalent pump power [83]. Compared to iterative design trials, NSGA-II has demonstrated exceptional capability in identifying optimal configurations within high-dimensional design spaces.

However, previous studies have primarily combined optimization algorithms with CFD, which demands substantial time and computational resources, reducing the efficiency of heat sink optimization. Recently, machine learning algorithms and modeling techniques—such as neural networks (NN), decision trees (DT), random forests (RF), gradient boosting (GB), adaptive neuro-fuzzy inference systems (ANFIS), and support vector machines (SVM)—have garnered increasing attention and are considered promising methods for analyzing thermal systems [84-85]. Neural networks (NN), which mimic brain-like processing to build various neural network models, can process extensive data to yield optimal results [86-89]. Compared to traditional CFD-based optimization approaches, NNs can rapidly predict heat dissipation performance under different design parameters by learning from large datasets, significantly reducing the need for CFD simulations and accelerating the optimization process. Almahmmadi et al.

[90] conducted a numerical study on the thermal performance of spiral coils, comparing artificial neural network (ANN) predictions with CFD results. Maximum differences in Nusselt number and friction values were only 9.6% and 0.1-9.7%, respectively, demonstrating ANN's high prediction reliability. Li et al. [91] used a backpropagation NN combined with multi-objective optimization to design microchannels with dual delta-wing vortex generators, achieving optimal fluid-thermal performance at high temperatures. Results indicated that the NN optimized via GA exhibited superior generalization and prediction for Nusselt number and friction factor compared to traditional NN. Ma et al. [92] developed an improved workflow for MCHS optimization, integrating analytical expressions with surrogate models and objective optimization algorithms. Polat and Cadirci [93] trained a multi-layer ANN using inputs like angle, Reynolds number, and pitch-to-diameter ratios of longitudinal and transverse pin fins. The NSGA-II algorithm then used Nusselt and Poiseuille numbers from the trained surrogate model to obtain Pareto-optimal solutions. Recognizing hydraulic performance's impact on thermal efficiency, Nusselt number and friction factor were incorporated as hydraulic performance metrics [94]. Furthermore, Wang et al. [95] proposed a composite microchannel design with various cavity shapes and straight ribs, analyzing its heat transfer and flow characteristics through numerical simulation. Optimization via ANN and NSGA-II, using Nusselt and friction factors as metrics, revealed that rounded rectangular ribs provided the best overall thermal performance, with average  $\eta$  approximately 9.7% higher than that of models without straight ribs.

However, the neural network training process adopted in previous studies usually requires collecting a large number of labeled datasets from CFD [96-97], which inevitably increases the time cost [98]. Therefore, some special methods that balance the prediction accuracy and training dataset requirements have been explored [99-104]. Blum et al. [101] proposed a method to improve the performance of learning algorithms by using a large number of unlabeled samples when only a small number of labeled samples are available. Specifically, confident labeled data verified by two pre-trained classifiers are randomly selected and implemented into a pool, allowing cheap unlabeled data to expand a smaller labeled dataset. Chen et al. [102] also proposed a semi-supervised hybrid neural network (HNN) for signal integrity. This method feeds the unlabeled data after cross-validation of pre-trained deep neural network (DNN) and convolutional neural network (CNN) back to

HNN as input, thereby achieving dataset expansion based on limited labeled samples. Compared with the individual methods in the hybrid structure, the accuracy of DNN and co-trained semi-supervised regression methods increased by 32.29% and 20.73%, respectively, but the required pre-processed training data was reduced by 50%. Feng et al. [103] proposed a hybrid pin-fin microchannel heat sink (HPFMCHS) which is optimized by hybrid neural network and non-dominated sorting genetic algorithm (NSGA-II).

### 3 Research Methodology

#### 3.1 Physical model

Figure. 1 shows the hybrid pin-fin microchannel heat sink from various angles, which is developed from the structure proposed by Ansari et al [45]. It can be seen that the entire heatsink consists of microchannel segments and pin-fins area where pin-fins uniformly located. Note that the turbulator array producing vortices effect distinguishes the hybrid MCHS from conventional smooth architectures, and it brings about comprehensive improvement of thermal and hydraulic performance. In practice, multiple parallel channels are required in MCHS to cover all chips where heat dissipation is strongly required. To reduce time overhead caused by the full model, a unit of MCHS with dual channels, herein, is intentionally constructed. The coolant absorbs heat from the heat source placed beneath the heatsink when flowing from the inlet to the outlet, leading to a temperature rise. The overall length ( $L$ ) of the heatsink is set as 10 mm. As shown in Figure. 1(b), the outer height ( $H_{ch}$ ) and the inner height ( $H_{tot}$ ) of channel are designed as 0.7 mm and 0.5 mm, respectively. The height of the pin-fin remains the same as the inner height of the heatsink. As depicted in Figure. 1(c), the width of a half microchannel unit ( $W_{tot}$ ) is 0.6 mm and the lateral width of the channel ( $W_{ch}$ ) is 0.25 mm.  $L_{ch}$  denotes the length of segment of the rectangular microchannel, and its value is assigned as 4 mm. With regard to the pin-fin, the spacing between any two individuals with radius ( $r$ ) of 0.06 mm is set as 0.2 mm. In this way, the array with fifty pin-fins shapes the region characterizing the outer length ( $W_{ao}$ ) of 2.3 mm and the inner length ( $W_{ai}$ ) of 2 mm. Since integrated microsystems usually package multiple cores on a silicon substrate, multiple heat sources were designed in this study. As shown in Figure. 1(d), two chips with different power densities are divided along the central axis of the microchannel unit,

defined as high power heat source (HPHS) and low power heat source (LPHS), respectively, to simulate the undesirable phenomenon of uneven temperature distribution caused by multiple heat sources in actual integrated microsystems.

The described model of HPFMCHS is built on the platform of ANSYS Spaceclaim 2023R2. Considering the compatibility of processing, the material of the heatsink is set as silicon and the deionized water is applied as the coolant. The related material properties are listed in Table 1. Note that the temperature dependency of these material parameters has slight influence on the simulated results but would dramatically increase the simulation time. Therefore, these properties of materials are set as constant.

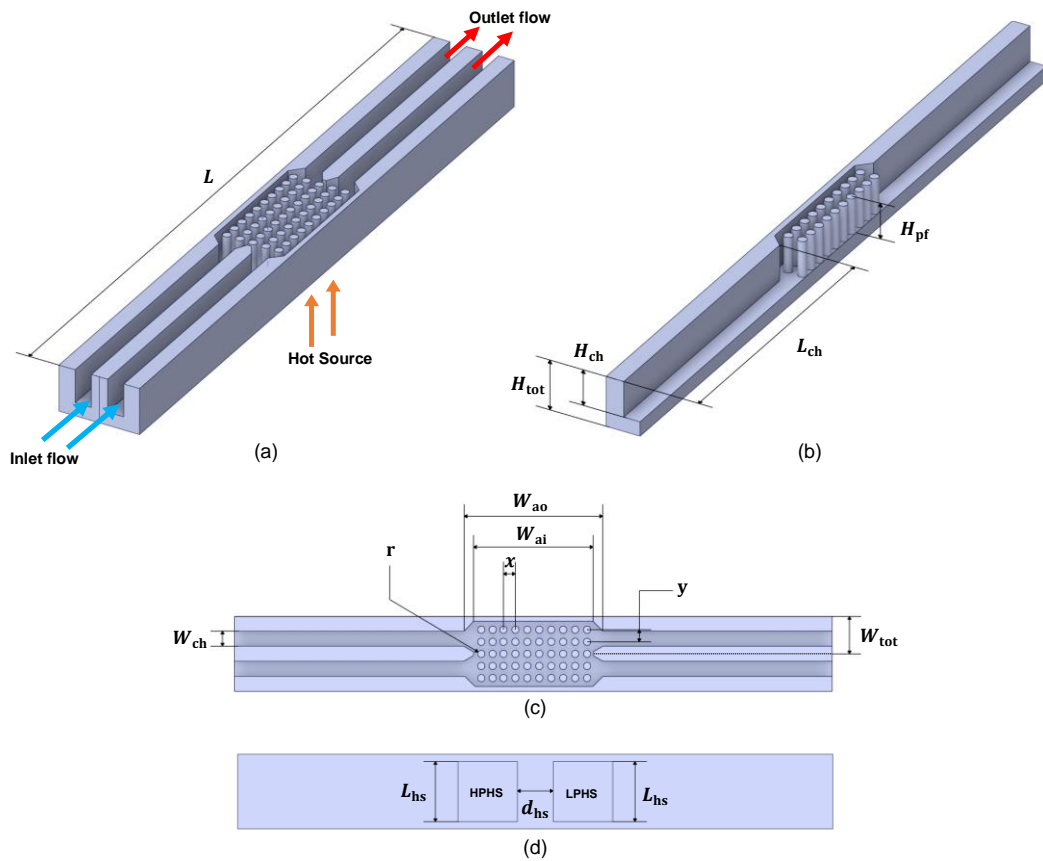


Figure 1. Schematics of (a) the overall view, (b) cross section view, (c) top view and (d) bottom view of a microchannel unit.

Table 1. Thermophysical properties of materials.

	$\rho$ ( $\text{kg} \cdot \text{m}^{-3}$ )	$c_p$ ( $\text{J} \cdot \text{kg}^{-1} \cdot \text{K}^{-1}$ )	$k$ ( $\text{W} \cdot \text{m}^{-1} \cdot \text{K}^{-1}$ )	$\mu$ ( $\text{kg} \cdot \text{m}^{-1} \cdot \text{s}^{-1}$ )
Solid	2329	712	148	-
Fluid	996.6	4178	0.609	$9.027 \times 10^{-4}$

### 3.2 Governing equations and boundary conditions

In order to perform accurate heat transfer and fluid flow simulation, reasonable assumptions of the numerical calculation conducted on ANSYS Fluent 2023R2 are made as follows:

- ✧ The default unit of the temperature is K and the pressure unit is kPa.
- ✧ The fluid is a three-dimensional stable laminar flow throughout the simulation.
- ✧ No phase change occurs during the liquid heat exchange process.
- ✧ The effects of gravity and thermal radiation conduction on the heat dissipation effect are ignored. The entire heatsink is set to be adiabatic.

The steady-state governing equations for the mass, momentum and energy in the fluid domain are provided as follows:

$$\nabla \cdot (\rho_f \bar{V}) = 0 \quad (1)$$

$$\bar{V} \cdot \nabla (\rho_f \bar{V}) = -\nabla p + \nabla \cdot (\mu \nabla \bar{V}) \quad (2)$$

$$\bar{V} \cdot \nabla (\rho_f C_p T_f) = \nabla \cdot (k_f \nabla T_f) \quad (3)$$

The energy equation in the solid domain is mathematically defined as:

$$\nabla (k_s \nabla T_s) = 0 \quad (4)$$

where  $\rho_f$ ,  $\mu$ ,  $C_p$ , and  $k_f$  are the density, dynamic viscosity, specific heat capacity, and thermal conductivity of the fluid, respectively,  $\bar{V}$  and  $T_f$  denotes the velocity and temperature of the fluid,  $p$  is the pressure, and  $k_s$  and  $T_s$  are the thermal conductivity and temperature of the heatsink (solid).

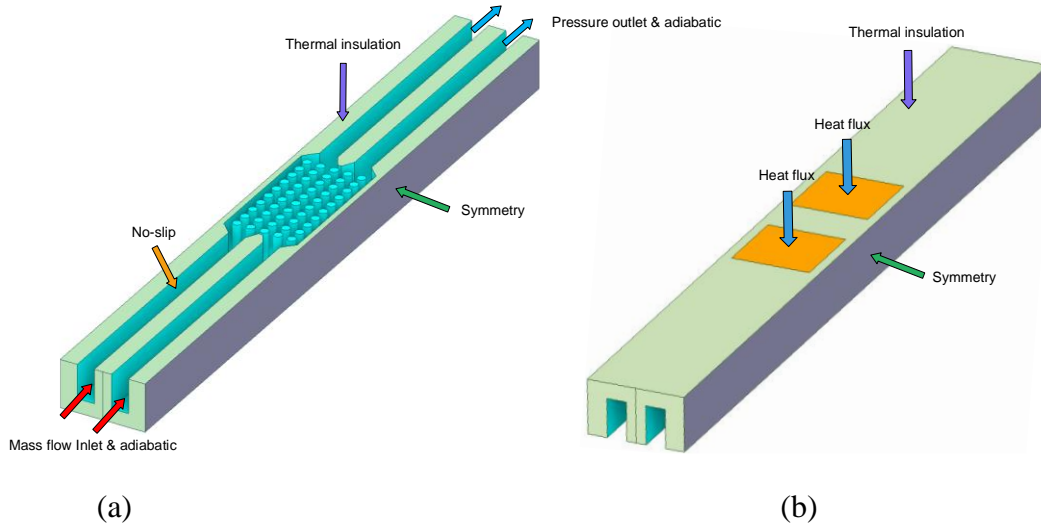


Figure. 2. Configuration of boundary conditions on the proposed HPFMCHS model. (a) top view and (b) bottom view

As shown in Figure. 2, to solve the equations, some necessary boundary conditions are configured as follows:

Due to the symmetry of the heat sink microchannel array, both side surfaces of the constructed microchannel unit are invoked as the boundary conditions of symmetry and periodicity:

$$\frac{\partial T_s}{\partial x} = 0 \quad (5)$$

A cover plate in glass is placed on the top of microchannel. Thus, solid wall and fluid wall are considered as thermal insulation as well as no-slip condition at the top of heatsink:

$$-k_s \frac{\partial T_s}{\partial n} = -k_f \frac{\partial T_f}{\partial n} = 0 \quad (6)$$

Adiabatic boundary conditions are adopted at the inlet and outlet of the microchannel:

$$k_s \frac{\partial T_s}{\partial n} = 0 \quad (7)$$

To ensure a fair comparison of the heatsink between different structures, the inlet is set as mass flow rate:

$$Q_m = \rho_f Q = \rho_f \bar{V} A_{ch} \quad (8)$$

where  $A_{ch}$  is the cross-sectional area of the microchannel unit and  $Q$  is the volume flow rate of coolant. In this work, the mass flow rate is fixed as  $7.47 \times 10^{-5}$  kg/h, and the initial temperature at the inlet is  $T_{in} = 293$ K.

The outlet of the microchannel is regarded as the pressure boundary condition. Due to the direct contact with air, the static pressure at the outlet is set as 0:

$$P = P_{out} = 0 \quad (9)$$

The power densities of the intentionally placed HPHS and LPHS are assigned as  $8 \times 10^2 \text{ W/mm}^2$  and  $4 \times 10^2 \text{ W/mm}^2$ , respectively [86].

$$-\frac{k_{s1}\partial T_{s1}}{\partial z} = q_1 = 8 \times 10^2 \text{ W/mm}^2 \quad (10)$$

$$-\frac{k_{s2}\partial T_{s2}}{\partial z} = q_2 = 4 \times 10^2 \text{ W/mm}^2 \quad (11)$$

At the solid-fluid coupling interface, the no-slip boundary condition is adopted:

$$u = v = w = 0 \quad (12)$$

$$T_s = T_f \quad (13)$$

$$-\frac{k_s\partial T_s}{\partial n} = -\frac{k_f\partial T_f}{\partial n} \quad (14)$$

### 3.3 Grid independence analysis

The numerical simulations require that the solid and fluid computational domains are discretized into volume elements, allowing the calculation process to be performed based on unstructured tetrahedral elements. Generally, in the fluid domain, multiple layers of high-precision hexagonal mesh elements are generated near the solid wall to ensure that the boundary layer of the flow can be resolved more accurately. In this work, a mesh independence analysis is discussed on the proposed HPFMCHS to eliminate the simulated error brought by the mesh quality. The number of meshes, dependent on the mesh size in the solid domain and the number of hexagonal mesh layers in the fluid domain, intentionally varies from 120,000 to 1.7 million. The focused critical indexes of the designed heatsink are shown in Figures. 3(a)-(b). It is evident that the accuracy of the simulation improves with the increased number of meshes and gradually converges when the number continually increases.

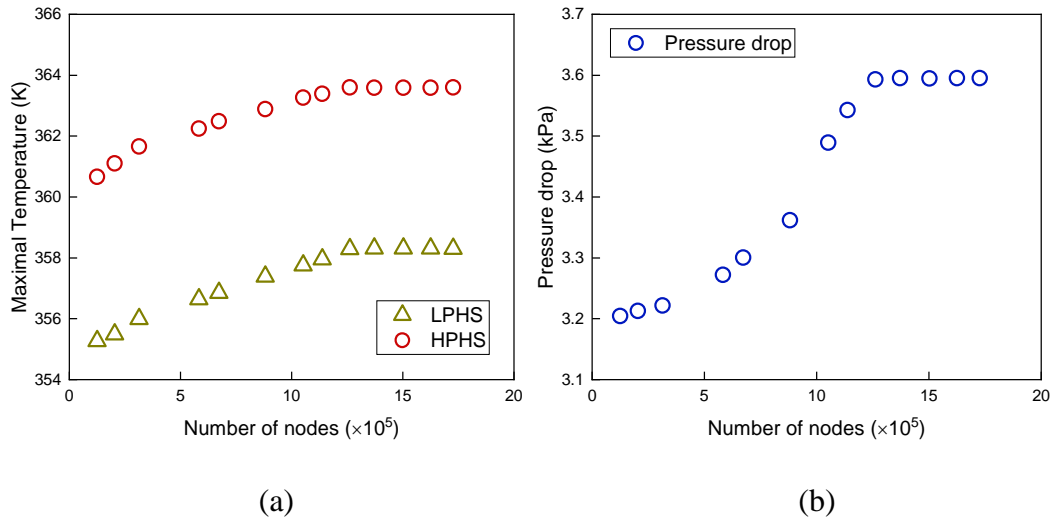


Figure. 3. Grid sensitivity tests of (a) the peak temperature and (b) pressure drop of the heatsink versus the number of mesh nodes.

However, this undoubtedly results in more time overhead. In order to balance the time cost and the accuracy, the mesh with 1.12 million is determined to be the trade-off, which is supported by the observed phenomenon that the maximum temperature variations of the HPHS and LPHS are only 0.35 K and 0.2 K when the number of the denser mesh further increases from 1.12 million to 1.7 million, as shown in Figure. 3(a). Likewise, a similar phenomenon is observed in Figure. 3(b) where the pressure drop of the hybrid heatsink fluctuates by a maximum of 0.053 kPa when the mesh density varies from 120,000 to 1.7 million. Therefore, the mesh with 1.12 million nodes is identified as the discretion method in the following simulations. Considering the efficiency in batch acquisition of temperature and pressure drop data sets, this study uses fluent mesh to mesh the entire heat sink instead of meshing each part separately. The computational mesh of the proposed HPFMCHS is illustrated in Figure. 4.

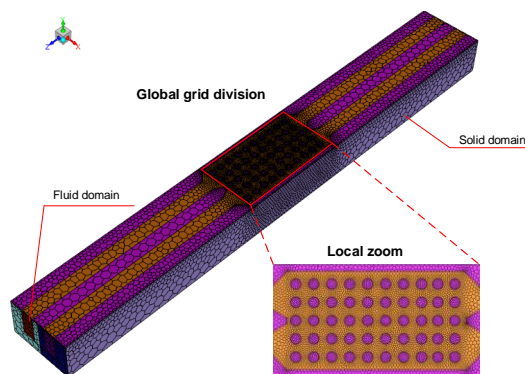


Figure. 4. Computational grid of proposed HPFMCHS.

### 3.4 Validation of numerical results

Ensuring the feasibility of the designed MPFMCHS and the accuracy of the CFD simulation, the simulated results are compared with the experimental results obtained from a previous literature by Wei et al. [105]. The validation is conducted on multilayer MCHS where the heat flux of the bottom chip is set as  $70 \text{ W/cm}^2$  and the flow rate at the top and bottom layers are  $0.5172 \text{ m/s}$  and  $0.4421 \text{ m/s}$ , respectively. In this way, nine sets of temperature values at intervals of  $0.1 \text{ m}$  along the entrance are firstly collected and compared with the experimental data in Figure. 5(a). At the same time, the corresponding comparison of pressure drop extracted from the CFD simulation and experiment is depicted in Figure. 5(b) [106]. The pressure drop of the microchannel is collected when the Reynolds number ranges from 140 to 951. The average absolute error of the temperature and pressure drop between simulation and experiment are quantified as  $0.43 \text{ K}$  and  $0.75 \text{ kPa}$ , respectively, demonstrating that the simulation in this work is confidently supported by the comparative result in both critical indexes.

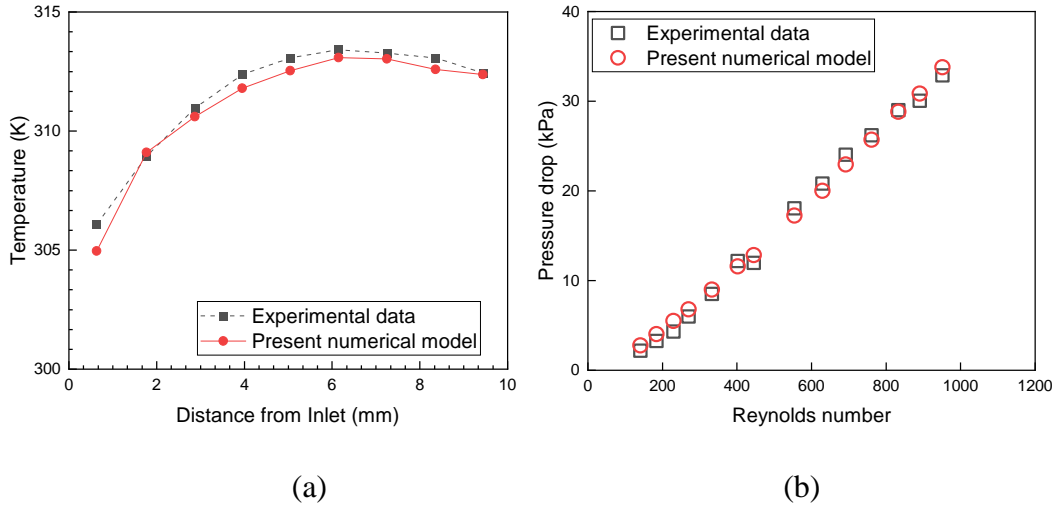


Figure. 5. Comparative results of (a) temperature from CFD simulation and experiment conducted by Wei et al. [105] and (b) pressure drop from simulation and experiment conducted by Qu and Mu-dawar [106].

### 3.5 Hybrid neural network

As aforementioned, the training process of NNs based on supervised learning requires a large amount of labeled data. However, the collected data, simulated from the computationally intensive CFD calculation, imposes limitations on the practicality and scalability of NNs. In contrast, semi-supervised learning offers a fashion to alleviate the

dependency on the known labeled datasets and facilitates the reduction of collection cycles. The concept of semi-supervised learning is between unsupervised learning featuring no labeled data and low accuracy and supervised learning featuring considerable labeled data and high accuracy. Usually, the verified unlabeled data is expanded into the labeled dataset, which greatly improves the data diversity and predicting accuracy of the trained NN prediction under small amount of the owned datasets. In this work, a HNN consisting of a DNN and a CNN is developed to map the underlying relationship between the identified structural parameters and critical performance indicators including maximum temperatures of two chips and overall pressure drop. Figure. 6 presents the working principle of the HNN, with the detailed implementation procedures illustrated as follows:

- (1) Pre-training of two NNs: the radius and height of the pin-fin, the lateral and longitudinal spacings between two pin-fins, and the width of microchannel are determined as the contributory parameters. The CFD simulation is performed to construct the labeled set  $L = \{(X_i, Y_i)\}$  where two subsets  $L_d$  and  $L_c$  are sampled to pre-train two embedded NNs before the first iteration.
- (2) Generation of the unlabeled dataset: In the first iteration, the unlabeled input set  $U = \{(X_i)\}$  is fed to the pre-trained DNN and CNN and the obtained outputs are labeled as  $Y_i^d$  and  $Y_i^c$ , respectively. The Euclidean distance is applied as the cross-validation criterion of them and mathematically calculated as  $L_{yh} = Y_i^d - Y_i^c$ ,  $i = 1, 2, \dots, N$ . In this work, the value of Euclidean distance is defined as 0.1. Following, the legal data  $U_s^d$  and  $U_s^c$  meeting the requirement of Euclidean distance is filtered from the predicted dataset  $U_d$  and  $U_c$  and randomly sampled with a sampling rate  $\alpha$  to build the supplementary data  $U_s^{d'}$  and  $U_s^{c'}$ . Finally, these obtained data are poured into the pool of the original labeled dataset.
- (3) Secondary validation and improved training: Based on the expanded dataset, DNN and CNN are independently trained with the updated datasets  $L_d$  and  $L_c$ . Note that the augmentation of the dataset does not necessarily guarantee an improvement in the accuracy of the NN training, while the dataset has been updated. Thus, the predicted performances of both NNs are examined to decide whether the added data should be saved or not.

The iterative process, comprising steps (2) and (3), always starts regardless of the effectiveness of the expanded dataset until the convergence threshold is reached. After obtaining the final iterative HNN model, 50 additional data points are used to test the regression ability of the model. In addition, root mean square error (RMSE), mean absolute error (MAE), and relative error (RE) are jointly used to measure the accuracy of the prediction.

The RMSE, MAE, and RE are defined as:

$$\text{RMSE} = \sqrt{\frac{1}{n} \sum_{i=1}^n (y_i - \hat{y}_i)^2} \quad (15)$$

$$\text{MAE} = \frac{1}{n} \sum_{i=1}^n |y_i - \hat{y}_i| \quad (16)$$

$$\text{RE} = \frac{|y_i - \hat{y}_i|}{y_i} \times 100\% \quad (17)$$

where  $n$  is the number of the sample,  $\hat{y}_i$  denotes the predicted value, and  $y_i$  is the actual value.

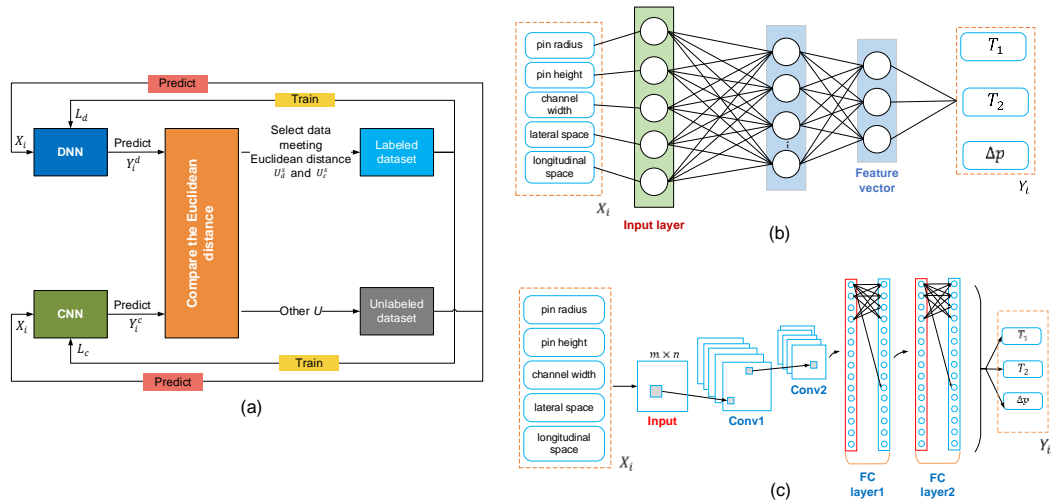


Figure. 6. (a) Flowchart of HNN and the structures of (b) CNN and (c) DNN.

### 3.6 Labelled dataset construction

The model of the pin-fin array is built and used to collect the original labelled dataset. The critical parameters to be designed are shown in Figure. 7(a). A total of 28 parameters are considered as the input variables of the collected dataset: four width variables of the

inlet and outlet canals ( $W_{ch1}, W_{ch2}, W_{ch3}, W_{ch4}$ ), two height ( $h_1, h_2$ ) and two radius variables ( $r_1, r_2$ ) of pin-fins in group1 and group2, ten lateral spacings ( $dx$ ) of pin-fins in each column, and ten longitudinal spacings ( $dy$ ) of pin-fins in each row compared with the original structure in Figure. 1. The lateral distance between any pair of adjacent pin-fins in a column of pin-fin array is identical. The outputs of the dataset, i.e., the comprehensive evaluation indexes of the microchannel, are defined as  $T_1$ ,  $T_2$ , and  $\Delta p$ .  $T_1$  and  $T_2$  denotes the maximal temperatures corresponding to HPHS and LPHS, respectively, and  $\Delta p$  is the pressure drop across the HPFMCHS. Besides, it is remarked that the position of pin-fins should be planned in detail to avoid illegal physically overlapped cases when collecting the valid dataset. Figure. 7(b) gives the flowchart of the legal layout generation and the procedure is illustrated as follows.

The spacings between pin-fins in each row is assumed as  $0.2 + dx_i (i \in (1,10))$ ,  $dx_i \in (-0.05, 0.05)$  and the spacings between the adjacent rows is  $0.2 + dy_j (j \in (1,10))$ ,  $dy_j \in (-0.05, 0.05)$ . They are required to satisfy the following conditions:

$$0.2 + dx_i > 2 \times r \quad (i \in (1,10)) \quad (18)$$

$$0.2 + dy_{j+1} - dy_j > 2 \times r \quad (j \in (1,10)) \quad (19)$$

Besides, in order to ensure that all pin-fins are within the design region of  $1 \text{ mm} \times 2 \text{ mm}$ , it is necessary to meet the following conditions:

$$\sum_{i=1}^5 0.2 + dx_i < 1 \quad (20)$$

$$\sum_{j=1}^{10} 0.2 + dy_{j+1} - dy_j < 2 \quad (21)$$

According to the above constraints, the matrix  $d$  related to the layout of pin-fin array is automatically generated using MATLAB. They are arranged for the CFD simulation to get the inputs of multiple structural parameters and the outputs including the peak temperatures of the LPHS and HPHS and the total pressure drop of the microchannel in steady state.

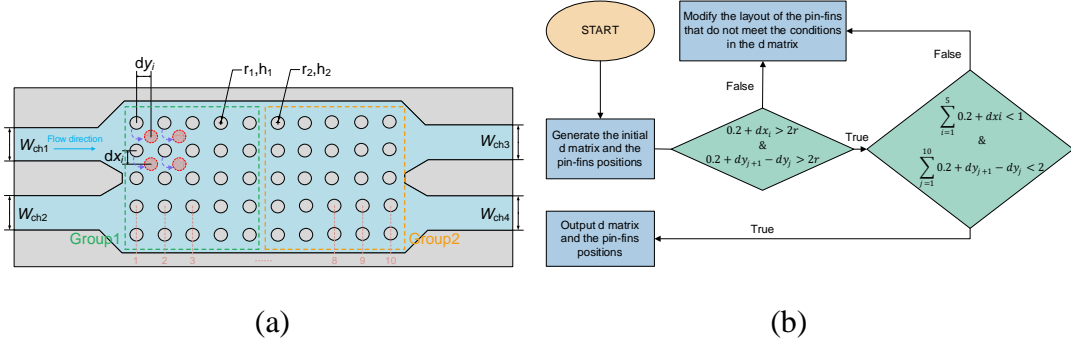


Figure. 7. (a) The variables to be optimized and (b) the flowchart of the legal layout generation of pin-fin array.

### 3.7 Multi-objective non-dominated sorting genetic algorithm optimization

To balance thermal and hydraulic performance of the designed HPFMCHS, NSGA-II is utilized as the driven optimization algorithm. Increasing the flow rate with sophisticated microchannel design, generally, benefits the improvement of heat transfer performance and the thermal uniformity of the chip, but also produces a large pressure drop. In this way, the optimization of the multi-objective design work targeting the minimization of maximal temperature of HPHS ( $T_1$ ), maximal temperature of LPHS ( $T_2$ ) and  $\Delta p$  at a constant flow rate and chip power can be formulated as:

$$\text{Minimize } F(x) = (T_1(x), T_2(x), \Delta p(x))^T$$

$$\text{Subject to } d \leq d_m$$

where  $x = (x_1, \dots, x_n)^T$  is the  $n$ -dimensional vector of design variables in the decision space  $\mathbb{R}^n$ , and  $F(x)$  is the  $m$ -dimensional objective vector such that  $F(x) \in \mathbb{R}^m$ . Besides, constrained by the geometric features of  $d \leq d_m$ , all optimal solutions should be physically feasible, i.e., separated from each other. Minimizing  $T_1$  and  $T_2$  was chosen as the optimization target as the chip temperature is critical to its performance, stability, and life. High temperature can affect the chip's computing speed, causing data processing delays or errors, and may also cause physical damage and shorten the chip's life. In addition, excessively high temperatures can accelerate phenomena such as electromigration, increase the risk of failure, and even cause system crashes or damage. In order to ensure that the chip operates efficiently and reliably while reducing energy consumption, it is very necessary to maintain reasonable temperature control. The multi-

objective optimization is performed subject to certain restrictions. As shown in Figure. 8, the flowchart of the developed NSGA-II is implemented using Python. For the designed HPFMCHS, 28 design variables mentioned in subsection 2.7 are considered during the optimization process. The multi-objective GA used in this work consists of the following 7 steps.

- Initialization: The arrangement algorithm depicted in Figure. 7 is used to generate the microchannels embedded with rectangular channels of different sizes and randomly distributed non-overlapping pin-fin array. According to the defined population size  $N$ , an equal number of the structural parameters set is used as the initial population of the iterative GA. Then, simulating the base pairs in biological genes, the corresponding value of the variables is binary-encoded.
- Fitness evaluation: In each iteration, three objective values are obtained to evaluate the quality of individuals. It is worth noting that the focused performance indexes are extracted from the trained HNN rather than conventional CFD simulations.
- Non-dominated sorting: The introduced crowding distance is computed based on the fitness values of all individuals, enabling the individuals in the population non-dominated sorted quickly. This avoids relying solely on a single indicator for ranking, thereby promoting performance balance and diversity design of HPFMCHS.
- Selection: Based on the arranged crowding distance, the tournament strategy, among two randomly selected members, is implemented to filter the advantageous one who is permitted to enter the evolution operation.
- Evolution: As the core of NSGA-II, this step allows the offspring to inherit partial genes from the arranged parent individuals through the operators of crossover and mutation. Wherein, the crossover between two individuals means that two gene segments between two randomly generated crossover points swap with each other. The mutation appears as the exploration of unknown areas in solution space, which is achieved by randomly changing at one or more certain gene loci. Then, the fitness value of each individual in the population is calculated again.
- Convergence: The process except the initialization step iterates until the termination condition of maximum iteration is met. Finally, the optimal Pareto front solution comprising non-dominated individuals is obtained. Note that the individuals in the Pareto front must possess two characteristics according to the non-dominated rule.

On one hand, three indicators  $T_1$ ,  $T_2$  and  $\Delta p$  are all improved compared with those of the initial design. On the other hand, at least one indicator is superior to all the remaining individuals for any given individual, but the case where three indexes are superior is forbidden in the non-dominated sorting.

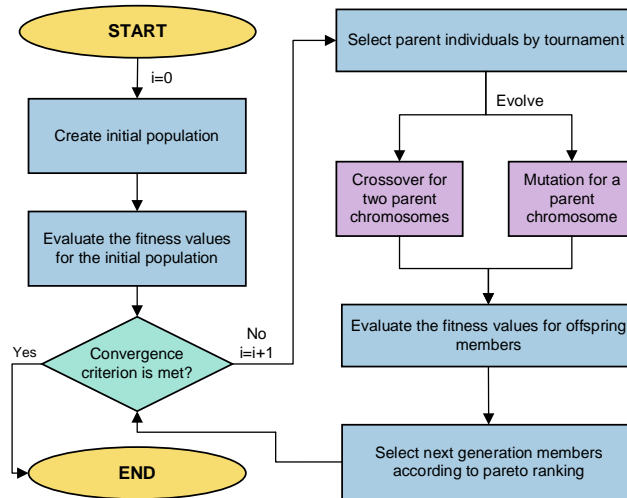


Figure. 8. Flowchart of the NSGA-II.

## 4 Results

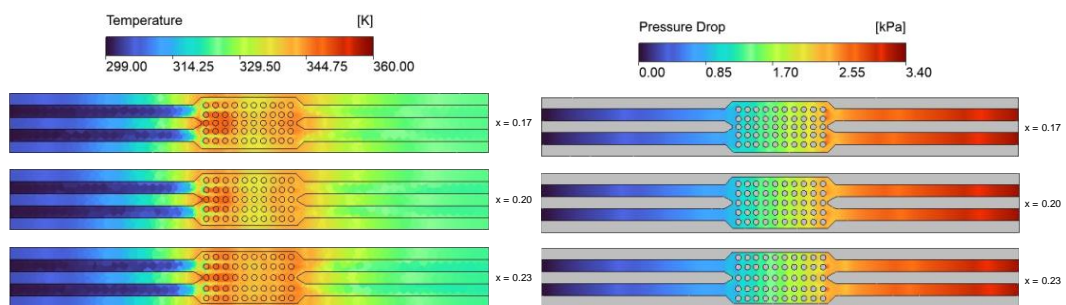
Based on the aforementioned approaches and specific settings for the design of HPFMCHS, the relevant results are presented and discussed in this section. Firstly, the effects of five categories of parameters classified from the mentioned 28 variables, including the width of the microchannel, the radius, height and distance of the pin-fin array at different positions on the thermal and hydraulic performance, are analyzed based on the initial hybrid structure. When one parameter is changed, the other parameters remain unchanged. Besides, the regression accuracy of the trained HNN is examined and compared with that of the conventional NN. At last, the developed NSGA-II provides the Pareto front solution where the optimal HPFMCHS with trade-off thermal and hydraulic performance is identified.

### 4.1 Comparison of different design paraments

#### 4.1.1 Lateral spacing between pin-fins

Based on the initial HPFMCHS shown in Figure. 1, the effect of the spacing perpendicular to the direction of flow on the temperature distribution and pressure drop is shown in Figures. 9(a)-(b). It is evident that the heat accumulation occurs in the pin-fin spacing

area when the pin-fin spacing decreases, but the overall accumulation phenomenon of the heatsink is lower than that in the case of large spacing. Observed from the temperature distribution diagram, the temperature of the coolant is lower after it flows out of the pin-fin array area when the spacing is 0.17 mm because the full heat exchange mainly occurs at the large interface between the fluid and the microchannel wall. In contrast, the temperature is high when the interval is 0.23 mm, indicating that the heat exchange is not sufficient. The phenomenon observed in the temperature profile can also be reflected in the velocity streamlines in Fig 9(c). It is found that the streamlines passing through the middle of the pin-fin array are denser when the spacing is 0.23 mm, which means that the pin-fin array has a weaker influence on the fluid diversion, thereby resulting in the concentrated flow through the middle of the pin-fin array. In contrast, when the spacing is 0.17 mm, the fluid is diverted in all directions due to the diversion effect of the pin-shaped fins, and the corresponding streamline distribution is more uniform. There is uniform heat exchange between the fluid and the microchannel wall when the fluid is evenly diverted and considerable heat is absorbed from the surface of the microchannel rather than the pin-fin. In terms of the pressure drop in Fig 9(b), it can be seen from the pressure distribution that there is a large pressure difference at the outlet of the pin-fin array when the lateral distance is 0.23 mm. This contributes to the large velocity difference formed between the middle of the pin-fin and the outlets caused by the large lateral distance. However, although the lateral interval is set as a small value of 0.17 mm, the above phenomenon of pressure drop is still observed. From the velocity cloud map, it is found that the fluid is blocked by the pin-fin with the decreased lateral interval, resulting in an increase of fluidic resistance from the inlet to the outlet. Besides, the pressure cloud map shows that the pressure drop in the pin-fin array gradually increases but still causes a relatively large pressure drop. Therefore, it is critical to find a balance point for the lateral distance between pin-fins that affects the thermal and hydraulic performance.



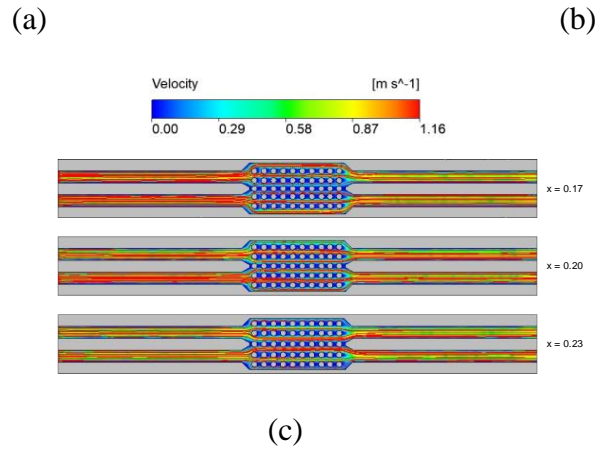


Figure. 9. Field distributions of (a) temperature, (b) pressure, and (c) velocity when  $Re = 200$  for different lateral spacing of pin-fins.

Figures. 10(a) and 10(b) present the maximum temperatures along with the steady-state pressure drop of the channel of HPHS and LPHS when lateral spacings rang from 0.17 mm to 0.23 mm. It is observed that at spacings of 0.17 mm and 0.20 mm, the maximum temperatures of HPHS and LPHS exhibit local minimum, while a spacing of 0.18 mm offers a local optimal solution for the overall pressure drop. Specifically, when the spacing is 0.17 mm, heat accumulation occurs in the temperature of the pin-fin array area, and the microfluid mainly exchanges heat with the channel wall in the array area. When the spacing is 0.20 mm, the heat accumulation in the pin-fin array area is reduced, and the fluid mainly exchanges heat with the pin-fin array area and the channel wall area. When the spacing is 0.23 mm, the temperature in the heat source area rises again. Combined with the velocity streamlines, when the spacing is 0.17 mm, the diversion effect of the pin-fin forces most of the fluid to flow through the channel wall and heat exchange occurs. When the spacing is 0.20 mm, the arrangement density of the pin-fin array decreases, and the shunting effect of the pin fins makes the fluid evenly distributed between the array and the channel wall, thereby increasing the heat exchange area between the fluid and the pin fins. However, due to the shunting of the pin fins, the bright blue area in the figure increases, indicating that the overall flow rate of the fluid is accelerated, making it impossible for the fluid to fully exchange heat with the channel wall and the pin fins, so the temperature is almost the same as the case of 0.17 mm spacing. When the spacing is 0.23 mm, the streamlines passing through the middle of the pin-fin array are denser, the guiding effect of the pin fins is weaker, the fluid flows quickly through the middle of the pin-fin array, and the fluid flowing through the microchannel wall is reduced, resulting in a decrease in the heat exchange area and an increase in the

hot spot temperature. Therefore, local minima will be generated at 0.17 mm and 0.20 mm. In conclusion, the lateral spacing of the pin-fin is a dominant parameter for the focused performance. The observed local trend of the chip temperature-lateral spacing distance curve motivates us to find the global optimal solution when the parametric range is expanded.

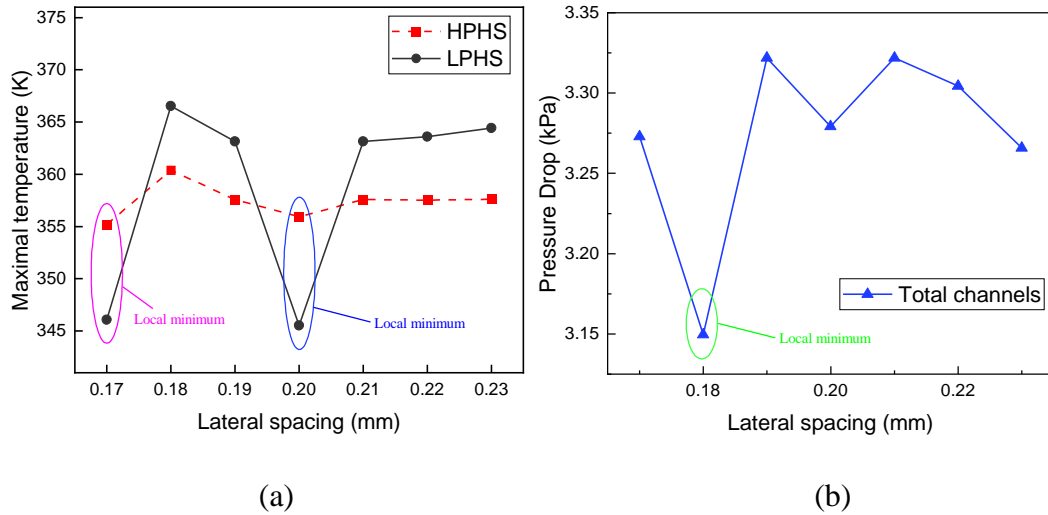


Figure. 10. Effects of lateral spacing of pin-fins on (a) peak temperature of chips and (b) the pressure drop.

#### 4.1.2 Longitudinal spacing between pin-fins

The temperature profile and pressure drop versus the longitudinal spacing of pin-fins are shown in Figure. 11(a) and 11(b). In Figure. 11(a), it can be seen that when the pin-fin longitudinal spacing decreases, heat accumulation occurs in the pin-fin spacing area. When the pin-fin spacing is 0.2 mm, the temperature of the chip and the heat sink reaches the lowest. Combined with the velocity streamlines in Figure. 11(c), compared with the case where the lateral spacing is 0.2 mm, the streamlines flow through the pin-fin array is delayed and the fluid is not divided until it contacts the pin-fin when the spacing is 0.17 mm. Therefore, the distance that most of the fluid flows through the pin-fin array is shortened, which alleviates the contact distance and the heat exchange between the fluid and the microchannel wall. When the spacing is increased to 0.23 mm, the microfluid is separated in advance before flowing into the pin-fin array. However, it can be seen from the velocity cloud map that the microfluid speed at this time is faster than that of 0.2 mm-distance pin-fin, which results in the inadequate heat exchange between the coolant and the pin-fin array. Thus, the cooling efficiency is significantly suppressed. As for the

pressure drop given in Figure. 11(b), there is a large pressure difference at the outlet of the pin-fin array when the lateral distance is 0.2 mm. This is attributed to the formed large speed difference between the middle outlets and both sides of the pin-fin. When the longitudinal spacing decreases to 0.17 mm, the reduced density of the pin-fin array leaves more room for the fluid flowing through the pin-fin array observed from the velocity cloud diagram.

The focused maximum temperature of two heat sources and corresponding pressure drop is shown in Figure. 12 where six groups of different longitudinal spacing are studied. It is evident that the temperatures are decreased sharply by 2.54 K and 18.08 K for HPHS and LPHS when the longitudinal spacing increases from 0.19 mm to 0.20 mm. This indicates the temperature curve exhibits a local minimum only at 0.20 mm. Regarding the pressure drop, a local minimum occurs at the longitudinal spacing of 0.17 mm. However, the maximum variation in pressure drop is 27 Pa when the longitudinal spacing is set between 0.18 mm and 0.23 mm, which implies the parametric steady state has been reached. In summary, the inconsistent impact of the longitudinal spacing on temperature and pressure drop implies that there will also exist corresponding global optima within a larger range of variables.

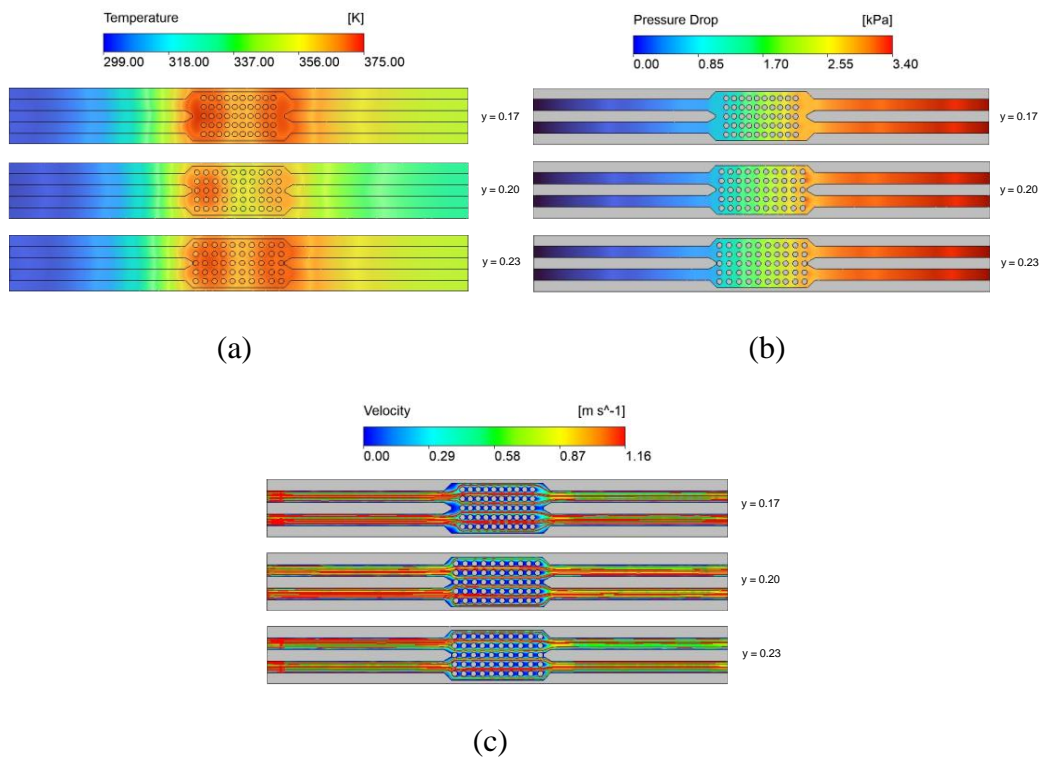


Figure. 11. Field distributions of (a) temperature, (b) pressure and (c) velocity when  $Re = 200$  for different pin-fin longitudinal spacing.

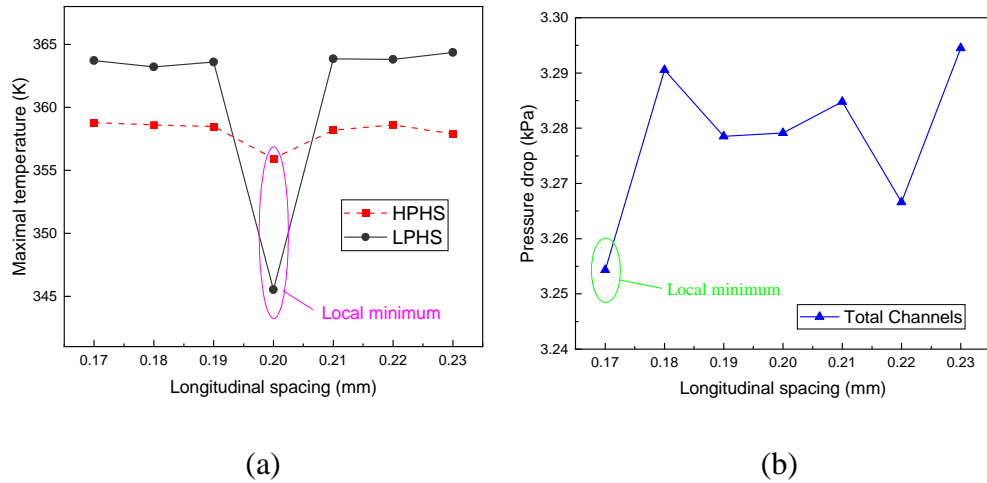
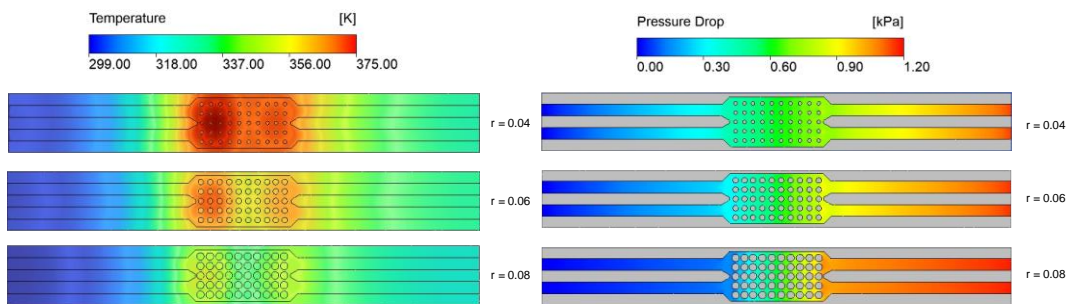


Figure. 12. Effects of longitudinal spacing on (a) peak temperature of chips and (b) pressure drop.

### 4.1.3 Radius of the pin-fin

The temperature profile and pressure drop influenced by the radius of key turbulators, i.e., pin-fin array, is exhibited in Figures. 13(a) and 13(b). The temperature map gets more uniform as the pin-fin radius increases simultaneously while minimizing the temperature of the region of heat sources. This can be explained by the velocity streamline distribution in Figure. 13(c). When the radius gradually gets larger, the original concentration of liquid within the array is partially transferred to both sides around the microchannel wall, resulting in the involvement of more regions in heat exchange brought by a more uniform distribution of the liquid. Therefore, the cooling efficiency is enhanced. Besides, the enhancement of the convective area between the liquid and pin-fin surface resulting from the increase of radius is considered as another important factor contributing to the improvement of heat dissipation efficiency. For the pressure drop, it is conceivable that an increase in radius leads to an enhanced obstruction capability of the pin-fin array to fluid flow. On one hand, it increases the pressure drop within the channels, and on the other hand, it accelerates the liquid velocity due to the squeezing effect.



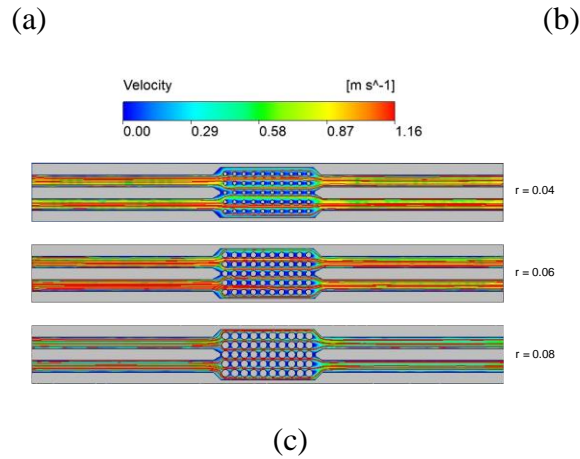


Figure. 13. Field distributions of (a) temperature, (b) pressure and (c) velocity when  $Re = 200$  for different pin-fin radius.

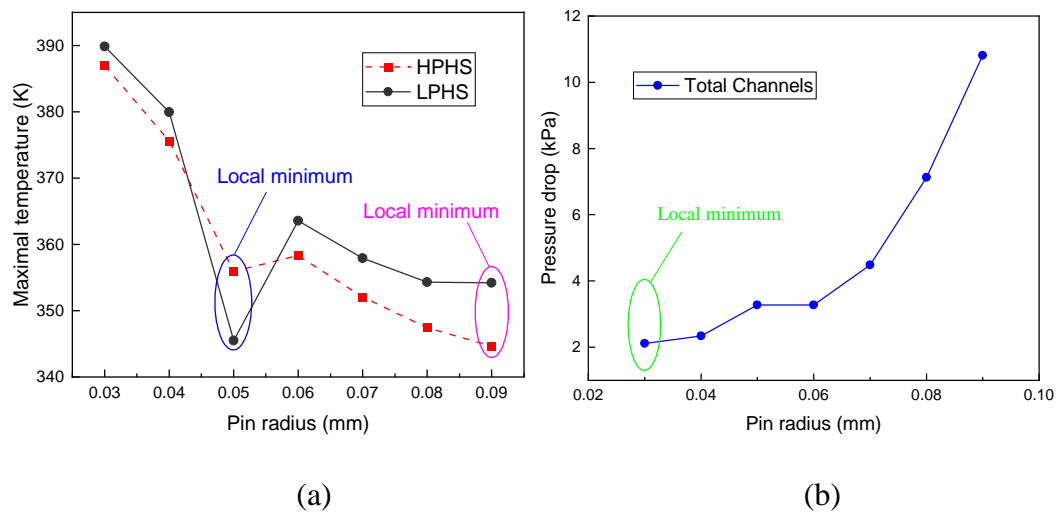


Figure. 14. Effect of pin-fin radius on temperature (a) and (b) pressure drop.

Figures. 14(a) and 14(b) present the quantitative evaluation of maximum temperatures as well as overall pressure drop in the microchannel. The temperature curve nearly monotonically decreases as the radius increases. Specifically, the temperature changes for HPHS and LPHS are calculated as 31.07 K and 44.32 K, respectively, between radii of 0.03 mm and 0.05 mm. Compared with 13.68 K and 9.34 K between 0.06 mm and 0.09 mm, the decreasing temperature variation indicates that the cooling capacity is no longer further promoted although the radius consistently increases. The curve in Figure. 14(b) shows the monotonical correlation between the pressure drop and the radius, and the increase rate becomes more pronounced when the radius exceeds 0.06 mm. This can be supported by that the increase rate is calculated 4.2 times in this range greater than that from 0.03 mm to 0.06 mm. Therefore, as the radius continues to increase, the resultant

inconsistent effects necessitate careful consideration in the balanced design of cooling performance and pressure drop.

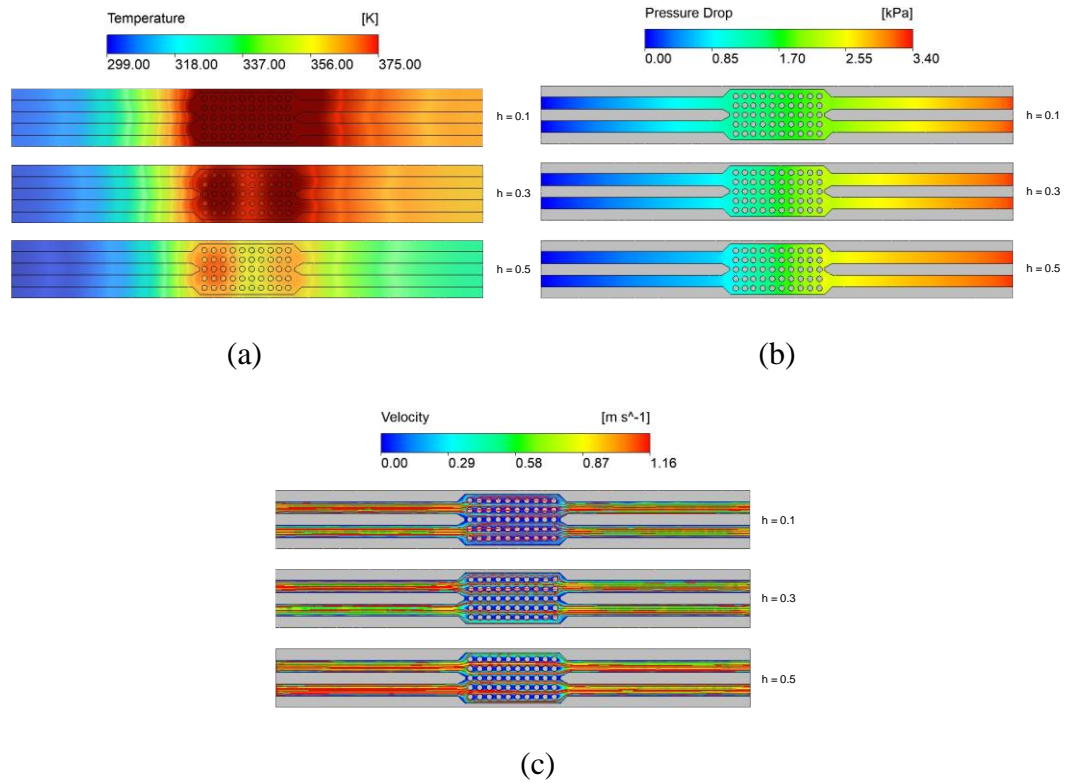


Figure. 15. Field distributions of (a) temperature, (b) pressure and (c) velocity when  $Re = 200$  for different pin-fin height.

#### 4.1.4 Height of the pin-fin

Figures. 15(a) and 15(b) present the distributions of maximum temperatures and pressure drop with different levels of pin-fin height. From the temperature distribution in Figure. 15(a), it is evident that the temperatures in the region of the heat sources decrease gradually with increasing pin-fin height, but pressure drops are found to increase as the height increases in Figure. 15(b). Both phenomena can be illustrated as follows. When the height is lower, there is an unobstructed cavity above the pin-fin array and more coolant can flow through the space. Due to the significant distance between the hot spot region and the concentrating flowing space, the efficiency of direct heat exchange is reduced. As the pin-fin height increases, the space is squeezed, while forcing the coolant to flow through the pin-fin array and improving heat exchange. Therefore, the cooling capacity exhibits a highly consistent variation trend with that of the pin-fin height. In contrast, the pressure drop exhibits an opposite trend due to the increased occupation brought by the larger volume of pin-fin array, thereby enhancing its resistance to liquid

flow and consequently leading to a greater pressure drop. Besides, the velocity streamline distribution in Figure. 15(c) provides support for this explanation. As the height increases, the denser streamline between pin-fin arrays indicates a greater volume of liquid passing through, which is consistent with the above discussion. Simulations are conducted on seven sets concerning the maximum temperature and pressure drop with respect to pin-fin height. The monotonic trends are more pronounced in Figure. 16, affirming the explanation provided above once again.

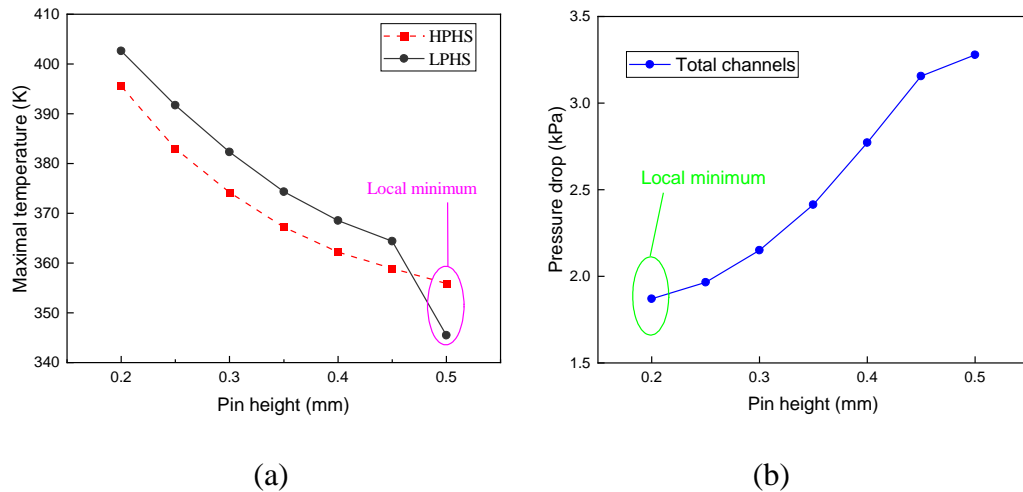
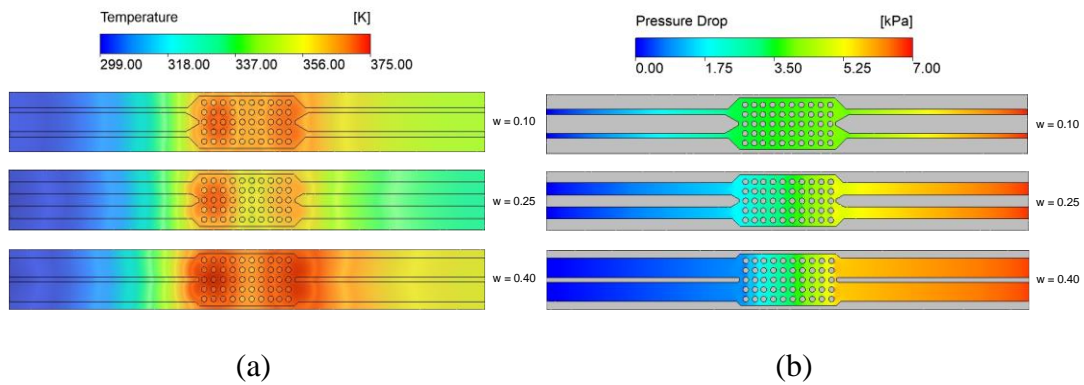


Figure. 16. Effect of pin-fin height on temperature (a) and (b) pressure drop.



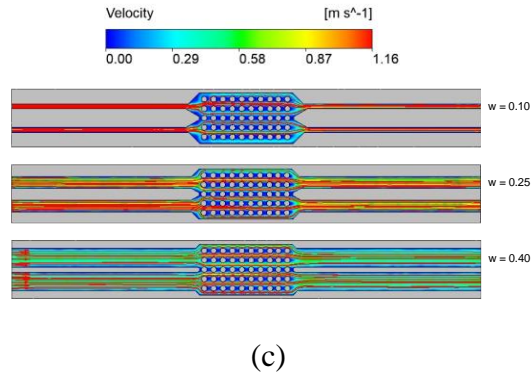


Figure. 17. Field distributions of (a) temperature, (b) pressure and (c) velocity at when  $Re = 200$  for different channel width.

#### 4.1.5 Width of the microchannel

The temperature and pressure drop distributions with respect to the width of the microchannel are shown in Figures. 17(a) and 17(b) where the inlet boundary conditions are maintained at the same mass flow rate. The overall temperature distribution shows an increasing trend with increasing width. Combining this with the velocity distribution shown in Figure. 17(c), liquid concentrates in the middle of the array at the inlet where high liquid velocity promptly carries the heat out of the channel due to the narrowness, replenishing it with cooler coolant when the width is 0.1 mm. When the channel width is 0.4 mm, the liquid velocity slows down and disperses into multiple areas, which hinders the timely removal of heat-absorbing liquid, thereby causing a temperature increase. However, when the channel width is 0.25 mm, a better balance is maintained between liquid velocity and distribution, resulting in sustained heat dissipation capabilities compared to narrower channel widths. The trend in pressure drop shown in Figure. 17(b) is relatively straightforward. As the channel width increases, the proportion of space occupied by the liquid distribution increases, leading to a smaller pressure drop. The phenomenon described above is more pronounced in the quantitative analysis depicted in Figure. 18. The peak temperatures of HPHS and LPHS exhibit an overall increasing trend with microchannel width. However, notably, a local minimum in maximum temperature occurs at 0.25 mm. This underscores the importance of intricate structural design, where certain specific dimensions can yield unexpected outcomes. The trend of pressure drop, as shown in Figure. 18(b), displays a strict monotonic relationship with channel width variation. Naturally, within this range, a local minimum in pressure drop occurs at the maximum channel width value.

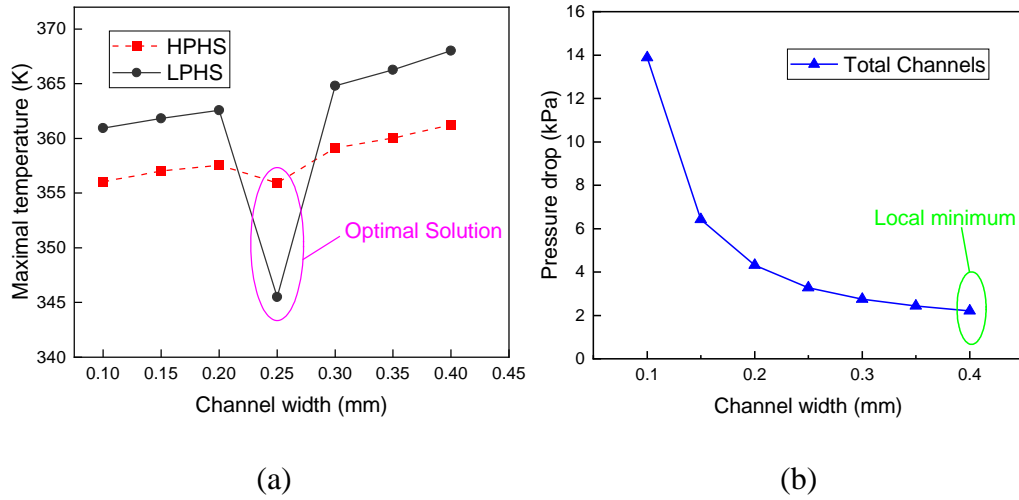


Figure. 18. Effect of channel width on temperature (a) and (b) pressure drop.

## 4.2 Hybrid NN Method

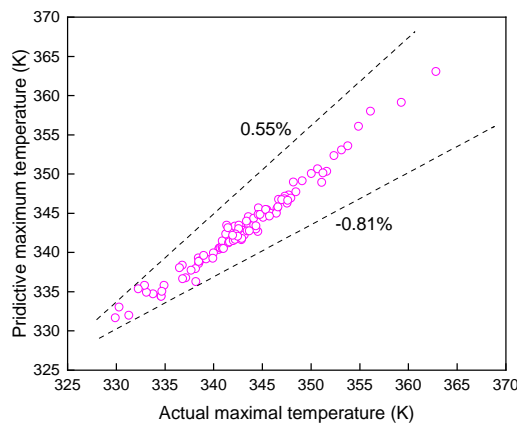
The deep learning model aims to learn patterns from training data that exhibit strong generalization capabilities, thereby improving its prediction or classification accuracy on unseen data. Generalization ability serves as an evaluation metric of the model's performance when handling unseen samples. Specifically, it reflects the extent to which the patterns learned from training data remain effective when applied to testing data or real-world applications. A model with good generalization ability is not only adept at handling training data but also adaptable to varying data distributions. In this study, the dataset is divided into a training set and a test set. First, 5000 design samples were generated within a specific parameter range, with duplicate samples removed to ensure the uniqueness of each set of parameters. Next, 1500 training samples and 100 test samples were obtained using Latin hypercube sampling. This approach not only ensures the independence of the training and test set samples, allowing for an effective evaluation of the model's generalization performance, but also guarantees a uniform and comprehensive distribution of the data.

In this subsection, the established HNN method is trained based on the generated 1500 groups of labelled datasets. During the training of the neural network, early stopping was employed. Training was halted when the model's performance on the validation set began to decline, preventing overfitting induced by continued training. The predictive accuracy calculated with 100 sets of non-repetitive test datasets is depicted in Figure. 19, which showcases the discrepancy between the actual and predicted data for the maximum

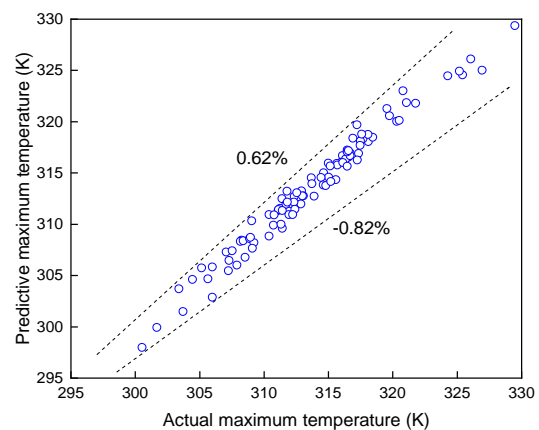
temperature of the heat sources and the pressure drop across the microchannel. The quantitative indexes of the performance evaluation are presented as follows: the prediction error range is  $-0.81\% \sim 0.55\%$  for the maximum temperature of HPHS,  $-0.82\% \sim 0.62\%$  for the maximum temperature of LPHS, and  $-5.67\% \sim 1.6\%$  for pressure drop. To validate the advantages of HNN aforementioned, two conventional supervised learning models, namely DNN [102] and CNN [104], are constructed. To ensure a fair comparison, the evaluation criterion that compares the comprehensive predictive error trained on the same number of labeled datasets is applied and corresponding indicators are listed in Table 2. It can be seen that HNN behaves better by  $\{93.4\%, 89.5\%, 87.8\%\}$  and  $\{91.7\%, 93.0\%, 91.9\%\}$  in terms of RMSE, MAE, and RE, compared with DNN and CNN. The relatively good prediction accuracy shows that HNN has significantly improved both accuracy and generalization ability.

Table 2: Comparison of predictive accuracy of the conventional CNN, DNN and the developed HNN

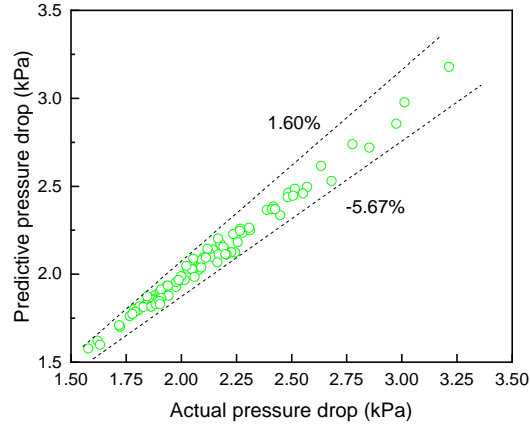
	RMSE	MAE	RE
DNN	10.15	3.53	0.02
CNN	8.06	5.28	0.03
HNN	0.67	0.37	0.0024



(a)



(b)



(c)

Figure. 19. Predictive error of HNN between predicted and actual values of (a) the maximal temperature of the HPHS, (b) the maximal temperature of LPHS and (c) the pressure drop in the microchannel.

### 4.3 Optimization with NSGA-II

In order to balance the hydraulic and thermal characteristics of HPFMCHS, NSGA-II is implemented to support the optimization work. In this study, due to the varying dimensions of the four rectangular channels in the heat sink, it is difficult to determine the hydraulic diameter, which complicates the calculation of  $Nu$  and  $f$ . Therefore, temperature and pressure drop are used as more direct and practical metrics. The identified 28 variables are treated as the input. The values of them, iteratively determined by the underlying rule of GA, are evaluated by the predictive performance indexes that HNN outputs. Based on the pre-optimization results, the population size and the number of the maximum iterations are designated as 100 and 170, respectively. The intermediate results of the Pareto front during the optimization are shown in Figure. 20. In the first generation, the distribution of the randomly generated population is relatively chaotic and the excellent individuals are mainly distributed at the moderate maximum level of the temperatures and pressure drop. After 5 generations of iteration, the target parameters of the population are found to converge to the lower left corner of the coordinate, which means that  $T_1$ ,  $T_2$ , and  $\Delta p$  gets smaller. By 15th generation, the feature of Pareto front curve is showcased, even if the distribution position is still not concentrated until 50th generation is reached. At this time, the target parameters are distributed more evenly, which is caused by the continuous enhancement of the crowding distance. The algorithm converges at 170th iteration where a curve of Pareto front is formed.

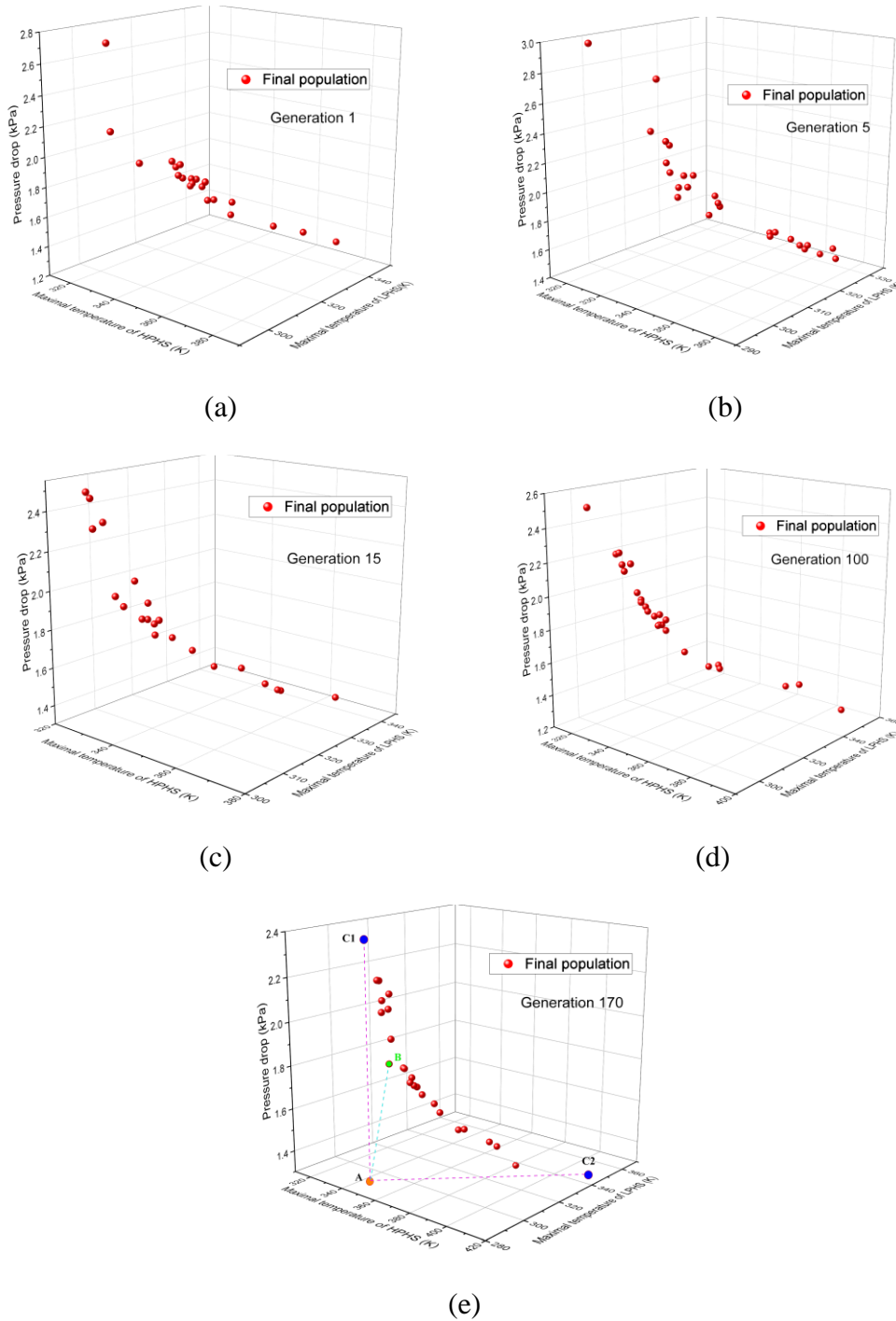


Figure. 20. Variations in temperature and pressure drop of (a) the first generation, (b) the fifth generation, (c) the fifteenth generation, (d) the one hundred-generation and (e) optimal decision point of Pareto front in the final generation population.

The Pareto front consists of multiple points, each sharing the common feature that none of their possessed performance parameters surpasses all those of any other point. This implies that an absolute optimal solution not exist in the provided Pareto front. Therefore, users are allowed to choose appropriate solution based on their design requirements. In this work, the optimization of a single performance aspect is not aggressively pursued,

but rather a well-balanced design solution that combines thermal performance and hydraulic performance is favored. To this end, a LINMAP-based method that searches the minimum Euclidean distance between the Pareto front and the ideal solution is selected to search for the final solution. According to the points C1 and C2 possessing the optimal value of single performance, the ideal solution denoted by the point A is determined, as shown in Figure. 20(e). However, it is not feasible to achieve three extremely optimal indicators marked as point A in the same structure. The received solution, obtained through the normalization ranking, is labeled as point B whose values are 336.02 K, 308.28 K, and 1.78 kPa, respectively. Additionally, considering that the structure is optimized based on the predictive performance parameters provided by HNN, CFD simulation is conducted to validate the optimization accuracy of the predictive model. The corresponding performance parameters are listed in Table 3, which indicates a high level of agreement between the HNN-based predictive parameters and the CFD simulated results. This further demonstrates the accuracy and effectiveness of the proposed HNN in accelerating the design process. Furthermore, a performance comparison is performed between the optimized structure and the initial one. The performance improvements of 4.27%, 7.68%, and 51.22%, brought by the NSGA algorithm are observed in terms of the peak temperatures of the HPHS and LPHS and the pressure drop, respectively.

Table 3. Comparison of temperature and pressure drop results between the initial and optimal HPFMCHS.

Method \ Value	Maximal temperature of HPHS (K)	Maximal temperature of LPHS (K)	Pressure drop (kPa)
Original Model	355.88	345.47	3.28
CFD-NSGA-II-Optimal	334.27(4.27% ↑)	310.94(7.68% ↑)	1.74(51.22% ↑)
HNN-NSGA-II-Optimal	336.02 (5.58% ↑)	308.28 (10.76% ↑)	1.78 (45.73% ↑)

The variables of the optimized structure are presented in Table 4, and the corresponding physical structure is shown in Figure. 21. It is evident that the pin-fin group beneath the

high-power heat source, adjacent to the channel inlet, has a larger radius. This configuration is beneficial for increasing the convective surface area to enhance the cooling of high-power heat source. Conversely, in the low-power heat source region, the unnecessary pin-fin radius is reduced to prevent excessive pressure drop. This in turn highlights the effectiveness of the selected design parameters.

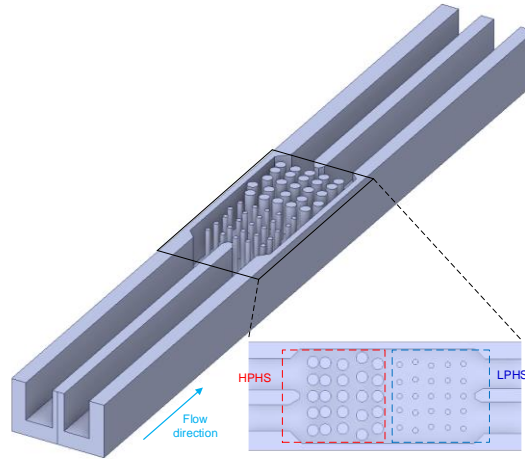


Figure. 21. Optimal structure of HPFMCHS.

Table 4. Optimal HPFMCH structure parameters

Parameter group	Value (mm)
r(pin radius)	(0.07,0.03)
h(pin height)	(0.50,0.49)
$dx_i$ (Lateral spacing change)	(-0.02,0.04,0.01,-0.01,0.01,-0.04,-0.02,0.01,0.04,0.03)
$dy_j$ (Longitudinal spacing change)	(-0.01,-0.02,-0.03,0.04,-0.04,-0.04,-0.01,-0.05,-0.04,-0.03)
$W_{ch}$ (Channel width)	(0.36,0.30,0.36,0.34)

## 5 Conclusion

In this work, a fast and intelligent design method combining a HNN and multi-objective NSGA was proposed to optimize the hybrid pin-fin heatsink. The impacts of multiple involved complex parameters on both thermal and hydraulic pressure drop performance were investigated. The contributory parameters were identified and arranged for the optimization work. A HNN approach, employed as a semi-supervised learning method,

was developed. Benefiting from the fast predictive capability inherent in NNs, the evaluation process of structural parameters traditionally conducted through CFD simulations was accelerated with a prediction accuracy of at least 94.33%. The predictive accuracy of this approach was compared with those of traditional supervised learning methods, such as DNN and CNN models. Under the same number of training datasets, an improvement of 93.4%, 89.5%, 87.8% and 91.7%, 93.0%, 91.9% was realized in terms of RMSE, MAE, and RE. Subsequently, NSGA-II was employed to optimize the critical parameters of the heatsink based on the performance indicators evaluated using the trained HNN. After optimization, the optimal values for the pin-fin's radius, height, lateral spacing, longitudinal spacing, and microchannel width were determined to be (0.07, 0.03), (0.50, 0.49), (-0.02, 0.04, 0.01, -0.01, 0.01, -0.04, -0.02, 0.01, 0.04, 0.03), (-0.01, -0.02, -0.03, 0.04, -0.04, -0.04, -0.01, -0.05, -0.04, -0.03), and (0.36, 0.30, 0.36, 0.34), respectively.

The final iteratively optimized structure was validated through CFD simulations, revealing a maximal temperature of 334.27K for HPHS, 310.94K for LPHS, and an overall heat sink pressure drop of 1.74kPa. Compared to the initial structure, the maximum temperatures of the HPHS and LPHS and pressure drop in the microchannel were improved by 5.58%, 10.76% and 45.73%. The successful application of HNN in the field of complex heat sink design, on the one hand, provides a reference for using NNs to replace repeated and complex CFD simulations in the heat sink optimization process. On the other hand, it solves the problem that using a single NN requires a large data set, while using CFD to obtain the data set is time-consuming. And with the continuous development of 3D-ICs and chiplet technology, multi-chip integration has made thermal management more challenging. The hybrid heat sink structure can cope with the situation of non-uniformly distributed heat sources, providing good thermal efficiency while improving the unevenness of heat distribution, which provides important guidance for the academic and engineering development in the field of integrated circuits.

## BIBLIOGRAPHY

- [1] S. K. Moore and D. Schneider, "The State of the Transistor: In 75 years, it's become tiny, mighty, ubiquitous, and just plain weird," in *IEEE Spectr.*, vol. 59, no. 12, pp. 30-31, Dec. 2022.
- [2] W. Aspray, "The Intel 4004 microprocessor: what constituted invention?" in *IEEE Annals of the History of Computing*, vol. 19, no. 3, pp. 4-15, July-Sept. 1997.
- [3] P.A. Merolla, J.V. Arthur, et al., "A million spiking-neuron integrated circuit with a scalable communication network and interface," in *Science*, vol. 345, pp. 668–673, Aug. 2014.
- [4] J. Parkhurst, J. Darringer, and B. Grundmann, "From single core to multi-core: Preparing for a new exponential," in *Proc. IEEE/ACM International Conference on Computer-Aided Design, Digest of Technical Paper (ICCAD)*, pp. 67–72, Feb. 2006.
- [5] B. Sinharoy et al., "IBM POWER7 multicore server processor," in *IBM Journal of Research and Development*, vol. 55, no. 3, pp. 1:1-1:29, May-June 2011.
- [6] E. Kursun and C. -Y. Cher, "Temperature Variation Characterization and Thermal Management of Multicore Architectures," in *IEEE Micro*, vol. 29, no. 1, pp. 116-126, Jan.-Feb. 2009.
- [7] K.N. Tu, "Reliability challenges in 3D IC packaging technology," in *Microelectron. Reliab.*, vol. 51, no. 3, pp. 517-523, Mar. 2011.
- [8] D. Deng, L. Zeng, W. Sun, "A review on flow boiling enhancement and fabrication of enhanced microchannels of microchannel heat sinks," in *Int. J. Heat Mass Transf.*, vol. 175, p. 121332. Aug. 2021.
- [9] L. Liu et al., "Optimization of 3-D IC routing based on thermal equalization analysis," in *IEEE Trans. Dev. Mater. Rel.*, vol. 24 no.2, pp. 250-259, June 2024.
- [10] L. Du, W. Hu, "An overview of heat transfer enhancement methods in microchannel heat sinks", in *Chem. Eng. Sci.*, vol. 280, p. 119081, Oct. 2023.
- [11] O. Semenov, A. Vassighi, M. Sachdev, "Impact of self-heating effect on long-term reliability and performance degradation in CMOS circuits," in *IEEE Trans. Dev. Mater. Reliab.*, vol. 6, pp. 17–27, Apr. 2006.

- [12] C. Bailey, "Thermal Management Technologies for Electronic Packaging: Current Capabilities and Future Challenges for Modelling Tools," in Proc. 2008 10th Electronics Packaging Technology Conference, Singapore, 2008, pp. 527-532.
- [13] L. Sauciuc, G. Chrysler, R. Mahajan and M. Szleper, "Air-cooling extension - performance limits for processor cooling applications," 9th Annual IEEE Semiconductor Thermal Measurement and Management Symposium, 2003., San Jose, CA, USA, 2003, pp. 74-81.
- [14] H. Feng et al., "Embedded Liquid Cooling of High-Power Microelectronics Using Liquid Metal," in Proc. 2024 IEEE 74th Electronic Components and Technology Conference (ECTC), Denver, CO, USA, 2024, pp. 1569-1574.
- [15] C. Hu, Z. Ma, Y. Zhang, X. Yang, X. Ma, J. Wei, "Optimizing the performance of microchannel heat sinks: Effects of trapezoidal cover plate on flow boiling heat transfer and stability," in *Int. J. Heat Mass Transf.*, vol. 244, 126942, 2025.
- [16] H. Cui, Z. Zhang, M. Yu, Z. Liu, W. Liu, "A hybrid slot jet impingement/microchannel heat sink for cooling high-power electronic devices: A combined experimental and numerical study," in *Int. J. Therm. Sci.*, 197, 108823, 2024.
- [17] J. Wang, C. Yuan, Y. Li, C. Li, Y. Wang, X. Wei, "Direct-to-chip immersion liquid cooling for high-power vertical-cavity surface-emitting laser (VCSEL)," in *Appl. Therm. Eng.*, vol. 269, Part B, 126137, 2025.
- [18] G. Wang, H. Ruan, H. Peng, Q. Xu, L. Lai, D. Xie, N. Neha, "Numerical investigation on hydrothermal performance of microchannel heat sink with impingement jet inlet arrays," *Int. C. Heat Mass Transf.*, vol. 165, Part A, 109013, 2025.
- [19] C. Li, X. Li, H. Huang, Y. Zheng, "Hydrothermal performance analysis of microchannel heat sink with embedded module with ribs and pin-fins", in *Appl. Therm. Eng.*, 225, 120167, 2023.
- [20] T. Wei, H. Oprins, V. Cherman, E. Beyne, and M. Baelmans, "Low-Cost Energy-Efficient On-Chip Hotspot Targeted Microjet Cooling for High-Power Electronics," in *IEEE Trans. Comp., Packag. Manuf. Technol.*, 10, pp. 577–589, 2020.

- [21] Z. Yang, X. Li, W. Zhang, T. Cai, W. Zhou, “Experimental and numerical simulation study of particles flow in the microchannel equipped with fan-shaped rib on sidewall,” in *Particuology*, vol. 100, pp. 45-61, 2025.
- [22] A. Shohdy, M. Emam, H. Sekiguchi, H. Hassan, “Performance of new hybrid heat sink with trimmed fins and microchannels for thermal control of a triple-junction concentrator photovoltaic cell,” in *Appl. Therm. Eng.*, 252, 123695, 2024.
- [23] M. Vargas-Santiago, D. A. León-Velasco, R. Monroy, “Resilient facility location optimization under failure scenarios using NSGA-III: A multi-objective approach for enhanced system robustness,” in *Exp. Syst. Appl.*, vol. 277, 127210, 2025.
- [24] S. Ranjan, R. Gupta, S. Nanda, “Threshold based constrained  $\theta$ -NSGA-III algorithm to solve many-objective optimization problems,” in *Inf. Sci.*, vol. 697, 121751, 2025.
- [25] W. Liu, J. Fang, S. Rolfo, C. Moulinec, D. Emerson, “An iterative machine-learning framework for RANS turbulence modeling,” in *Int. J. Heat Fluid Flow*, vol. 90, 108822, 2021.
- [26] Y. Zhang, J. Tang, Z. Cao, “Semi-supervised multi-label feature selection via partial label correlation and feature self-representation,” in *Knowledge-Based Syst.*, vol. 320, 113632, 2025.
- [27] D.B. Tuckerman, R.F.W. Pease, “High-performance heat sinking for VLSI,” in *IEEE Electron. Dev. Lett.*, vol. 2, pp. 126–129, May 1981.
- [28] P. Zając, C. Maj, A. Napieralski, “Peak temperature reduction by optimizing power density distribution in 3D ICs with microchannel cooling,” in *Microelectron. Reliab.*, vol. 79, pp. 488-498, Dec. 2017.
- [29] H.C. Cui, Z.K. Zhang, M.J. Yu, Z.C. Liu, W. Liu, “A hybrid slot jet impingement/microchannel heat sink for cooling high-power electronic devices: A combined experimental and numerical study,” in *Int. J. Therm. Sci.*, vol. 197, p. 108823, Mar. 2024.
- [30] B. Ding, Z.H. Zhang, L. Gong, M.H. Xu, Z.Q. Huang, “A novel thermal management scheme for 3D-IC chips with multi-cores and high power density,” in *Appl. Therm. Eng.*, vol. 168, no. 5, p. 114832, Mar. 2020.
- [31] H.J. Huang, L.M. Pan, R.G. Yan, “Flow characteristics and instability analysis of

- pressure drop in parallel multiple microchannels,” in *App. Therm. Eng.*, vol. 142, pp. 184-193, Sept. 2018.
- [32] R.V. Erp, R. Soleimanzadeh, L. Nela, G. Kampitsis, E. Matioli, “Co-designing electronics with microfluidics for more sustainable cooling,” in *Nature*, vol. 585, pp. 211–216, Sept. 2020.
- [33] C.Q. Li, X.B. Li, H.Y. Huang, Y.H. Zheng, “Hydrothermal performance analysis of microchannel heat sink with embedded module with ribs and pin-fins,” in *Appl. Therm. Eng.*, vol. 225, no. 5, p. 120167, May 2023.
- [34] Z. Feng, X. Luo, F. Guo, H. Li, J. Zhang, “Numerical investigation on laminar flow and heat transfer in rectangular microchannel heat sink with wire coil inserts,” in *Appl. Therm. Eng.*, vol. 116, pp. 597–609, Apr. 2017.
- [35] H.-L. Liu, D.-H. Qi, X.-D. Shao, W.-D. Wang, “An experimental and numerical investigation of heat transfer enhancement in annular microchannel heat sinks,” in *Int. J. Therm. Sci.*, vol. 142, pp. 106–120, Aug. 2019.
- [36] M. Yang, B. Cao, “Numerical study on flow and heat transfer of a hybrid microchannel cooling scheme using manifold arrangement and secondary channels,” in *Appl. Therm. Eng.*, vol. 159, p. 113896, Aug. 2019.
- [37] G. Lu, X. Zhai, “Analysis on heat transfer and pressure drop of a microchannel heat sink with dimples and vortex generators,” in *Int. J. Therm. Sci.*, vol. 145, p. 105986, Nov. 2019.
- [38] W. Ling, W. Zhou, C. Liu, F. Zhou, D. Yuan, J. Huang, “Structure and geometric dimension optimization of interlaced microchannel for heat transfer performance enhancement,” in *Appl. Therm. Eng.*, vol. 170, p. 115011, Apr. 2020.
- [39] A.Y.M. Ali, E.M. Abo-Zahhad, M.F. Elkady, S. Ookawara, A.H. El-Shazly, A. Radwan, “Temperature uniformity enhancement of densely packed high concentrator photovoltaic module using four quadrants microchannel heat sink,” in *Solar Energy*, vol. 202, no.15, pp. 446–464, May. 2020.
- [40] M. Peng, L. Chen, W. Ji, W. Tao, “Numerical study on flow and heat transfer in a multi-jet microchannel heat sink,” in *Int. J. Heat Mass Transfer*, vol. 157, p. 119982, Aug. 2020.

- [41] L. Lin, J. Zhao, G. Lu, X.-D. Wang, W.-M. Yan, "Heat transfer enhancement in microchannel heat sink by wavy channel with changing wavelength/amplitude," in *Int. J. Therm. Sci.*, vol. 118, pp. 423–434, Aug. 2017.
- [42] F.B. Abdul Hasis, P.M. Mithun Krishna, G.P. Aravind, M. Deepu, S.R. Shine, "Thermo hydraulic performance analysis of twisted sinusoidal wavy microchannels," in *Int. J. Therm. Sci.*, vol. 128, pp. 124–136, June 2018.
- [43] Y. Lei, Z. Chen, "Cooling heat transfer and pressure drop of supercritical CO<sub>2</sub> in wavy microchannels with consistent and opposite crests and troughs," in *Int. J. Refrig.*, vol. 109, pp. 64–81, Jan. 2020.
- [44] D. Sreehari, A.K. Sharma, "On thermal performance of serpentine silicon microchannels," in *Int. J. Therm. Sci.*, vol. 146, p. 106067, Dec. 2019.
- [45] D. Ansari, K.Y. Kim, "Hotspot thermal management using a microchannel-pin-fin hybrid heat sink," in *Int. J. Therm. Sci.*, vol. 134, pp. 27-39, Dec. 2018.
- [46] J. Tang, X. Li, R. Hu, Z. Mo, M. Du, "A novel designed manifold ultrathin micro pin-fin channel for thermal management of high-concentrator photovoltaic system," in *Int. J. Heat Mass Transf.*, vol. 183, Part. A, p. 122094, Feb. 2022.
- [47] L.L. Chen, G.A.B. Robin, W. Bernhard, P. Rico, Q.Z. Yang, "Detailed investigation of staggered jet impingement array cooling performance with cubic micro pin fin roughened target plate," in *Appl. Therm. Eng.*, vol. 171, no.5, p. 115095, May 2020.
- [48] G.D. Xia, J. Jiang, J. Wang, Y.L. Zhai, D.D. Ma, "Effects of different geometric structures on fluid flow and heat transfer performance in microchannel heat sinks," in *Int. J. Heat Mass Tran.*, vol. 80, pp. 439–447, Jan. 2015.
- [49] Q. Zhu, H. Xia, J. Chen, X. Zhang, K. Chang, H. Zhang, H. Wang, J. Wan, Y. Jin, "Fluid flow and heat transfer characteristics of microchannel heat sinks with different groove shapes," in *Int. J. Therm. Sci.*, vol. 161, p.106721, Mar. 2021.
- [50] H.E. Ahmed, M.I. Ahmed, "Optimum thermal design of triangular, trapezoidal and rectangular grooved microchannel heat sinks," in *Int. Commun. Heat Mass Tran.*, vol. 66, pp. 47–57, Aug. 2015.
- [51] N. Kumari, T. Alam, M.A. Ali, A.S. Yadav, N.K. Gupta, M.I.H. Siddiqui, D. Dobrořa, I.M. Rotaru, A. Sharma, "A numerical investigation on hydrothermal performance of

- micro channel heat sink with periodic spatial modification on sidewalls,” in *Micromachines*, vol. 13, no. 11, p. 1986, Nov. 2022.
- [52] Q. Zhang, Z. Li, Z. Feng, Z. Chen, J. Zhang, F. Guo, “Effects of combination modes of different cavities and ribs on performance in mini-channels a comprehensive study,” in *Int. Commun. Heat Mass Tran.*, vol. 142, p. 106633, March 2023.
- [53] A.S. Yadav, V. Shrivastava, T. Ravi Kiran, M.K. Dwivedi, “CFD-based correlation development for artificially roughened solar air heater,” in *Recent Adv. Mech. Eng.*, vol. 47, pp. 217–226, May 2021.
- [54] R. Prasad, A.S. Yadav, N.K. Singh, D. Johari, “Heat transfer and friction characteristics of an artificially roughened solar air heater,” in *Adv. Fluid Thermal Eng.*, pp. 613–626, Apr. 2019.
- [55] A.S. Yadav, S.K. Sharma, “Numerical simulation of ribbed solar air heater,” in *Adv. Fluid Thermal Eng.*, pp. 549–558, Apr. 2021.
- [56] A.S. Yadav, A. Agrawal, A. Sharma, S. Sharma, R. Maithani, A. Kumar, “Augmented artificially roughened solar air heaters,” in *Mater. Today*, vol. 63, pp. 226–239, Jan. 2022.
- [57] Z. Feng, C. Zhou, F. Guo, J. Zhang, Q. Zhang, Z. Li, “The effects of staggered triangular ribs induced vortex flow on hydrothermal behavior and entropy generation in microchannel heat sink,” in *Int. J. Therm. Sci.*, vol. 191, p. 108331, Sept. 2023.
- [58] M.S. Lori, K. Vafai, “Heat transfer and fluid flow analysis of microchannel heat sinks with periodic vertical porous ribs,” in *Appl. Therm. Eng.*, vol. 205, no. 12, p. 118059, Mar. 2022.
- [59] A.P. Dash, T. Alam, M.I.H. Siddiqui, P. Blechich, M. Kumar, N.K. Gupta, M.A. Ali, A.S. Yadav, “Impact on heat transfer rate due to an extended surface on the passage of microchannel using cylindrical ribs with varying sector angle,” in *Energies*, vol. 15, no. 21, p. 8191, Nov. 2022.
- [60] I. Haque, T. Alam, J. Yadav, N.K. Gupta, M.I.H. Siddiqui, T.U. Siddiqui, N. Ali, S. Srivastava, A.S. Yadav, A. Sharma, R. Khargotra, A.K. Thakur, “Numerical analysis of various shapes of lozenge pin-fins in microchannel heat sink,” in *Int. J. Chem. React. Eng.*, vol. 22, no. 1, Sept. 2023.

- [61] G.D. Xia, Y.T. Jia, Y.F. Li, D.D. Ma, B. Cai, “Numerical simulation and multiobjective optimization of a microchannel heat sink with arc-shaped grooves and ribs,” in *Numer. Heat Tran. A.*, vol. 70, no. 9, pp. 1041–1055, Apr. 2016.
- [62] A. Datta, V. Sharma, D. Sanyal, P. Das, “A conjugate heat transfer analysis of performance for rectangular microchannel with trapezoidal cavities and ribs,” in *Int. J. Therm. Sci.*, vol. 138, pp. 425–446, Apr. 2019.
- [63] Y.F. Yan, J.H. Wu, F.L. Xu, Y.R. Chen, Z.Q. He, “Experimental investigation on flow and heat transfer characteristics of the drop-pressure microchannel heat sink with gradient distribution pin fin arrays and narrow slots,” in *Appl. Therm. Eng.*, vol. 233, p. 121084, Oct. 2023.
- [64] S.A. Lawson, A.A. Thrift, K.A. Thole, A. Kohli, “Heat transfer from multiple row arrays of low aspect ratio pin fins,” in *Int. J. Heat Mass Transf.*, vol. 54, no. 17–18, pp. 4099-4109, Aug. 2011.
- [65] H.-C. Chiu, R.-H. Hsieh, K. Wang, J.-H. Jang, C.-R. Yu, “The heat transfer characteristics of liquid cooling heat sink with micro pin fins,” in *Int. Commun. Heat Mass Transf.*, vol. 86, pp. 174–180, Aug. 2017.
- [66] Z. Feng, Z. Hu, Y. Lan, Z. Huang, J. Zhang, “Effects of geometric parameters of circular pin-fins on fluid flow and heat transfer in an interrupted microchannel heat sink,” in *Int. J. Therm. Sci.*, vol. 165, p. 106956, July 2021.
- [67] W. A. Khan, J. R. Culham and M. M. Yovanovich, "Modeling of cylindrical pin-fin heat sinks for electronic packaging," in *Proc. Semiconductor Thermal Measurement and Management IEEE Twenty First Annual IEEE Symposium, 2005.*, San Jose, CA, USA, 2005, pp. 125-134.
- [68] A. Mohammadi, A. Kosar, “Hydrodynamic and thermal performance of microchannels with different staggered arrangements of cylindrical micro pin fins,” in *J Heat Transfer*, vol. 139, no. 6, Jun. 2017.
- [69] T. John, B. Mathew, H. Hegab, “Parametric study on the combined thermal and hydraulic performance of single phase micro pin-fin heat sinks part i: square and circle geometries,” in *Int. J. Therm. Sci.*, vol. 49, no. 11, pp. 2177–2190, Nov. 2010.
- [70] A. Sertkaya, M. Ozdemir, E. Canli, “Effects of pin fin height, spacing and orientation

- to natural convection heat transfer for inline pin fin and plate heat sinks by experimental investigation,” in *Int J Heat Mass Transf.*, vol. 177, p. 121527, Oct. 2021.
- [71] M. Vilarrubi, S. Riera, M. Ibañez, M. Omri, G. Laguna, L. Fréchette, J. Barrau, “Experimental and numerical study of micro-pin-fin heat sinks with variable density for increased temperature uniformity,” in *Int. J. Therm. Sci.*, vol. 132, pp. 424–434 Oct. 2018.
- [72] Y. Huang, M. Xu, H. Li, S. Shen, X. Song, H. Liu, A. Waili, L. Zhao, W. Wei, “Novel thermal design of micro-bream-fin heat sink using contour-extraction-based (CEB) method,” in *Int. J. Therm. Sci.*, vol. 165, p. 106952, July 2021.
- [73] M. Ahmadian-Elmi, A. Mashayekhi, S. Nourazar, K. Vafai, “A comprehensive study on parametric optimization of the pin-fin heat sink to improve its thermal and hydraulic characteristics,” in *Int. J. Heat Mass Transf.*, vol. 180, p. 121797, Dec. 2021.
- [74] M. Hekmatara, M. Kharati-Koopae, “Numerical study of the influence of pin fin arrangement and volume fraction on the heat transfer and fluid flow phenomena within open microchannels,” in *Int. Commun. Heat. Mass. Transf.*, vol. 155, p. 107595, June 2024.
- [75] Z. Li, Z. Feng, Q. Zhang, J. Zhou, J. Zhang, F. Guo, “Thermal-hydraulic performance and multi-objective optimization using ANN and GA in microchannels with double delta-winglet vortex generators,” in *Int. J. Therm. Sci.*, vol. 193, p. 108489 Nov. 2023.
- [76] F.B. Majmader, M.J. Hasan, “Multi-objective hydrothermal performance optimization of a microchannel heat sink equipped with delta winglet vortex generators using NSGA-II genetic algorithm,” in *Int. J. Therm. Sci.*, vol. 201, p. 109046, July. 2024.
- [77] N. Srinivas, K. Deb, “Multiobjective optimization using nondominated sorting in genetic algorithms,” in *IEEE Trans. Evol. Comput.*, vol. 2, no. 3, pp. 221-248, Sept. 1994.
- [78] L. Gosselin, M.T. Gingras, F.M. Potvin, “Review of utilization of genetic algorithms in heat transfer problems,” in *Int. J. Heat Mass Transf.*, vol. 52, no. 9–10, pp. 2169–

- 2188, Apr. 2009.
- [79] A. Yildizeli, S. Cadirci, “Multi objective optimization of a micro-channel heat sink through genetic algorithm,” in *Int. J. Heat Mass Transf.*, vol. 146, p. 118847, Jan. 2020.
- [80] K. Foli, T. Okabe, M. Olhofer, Y.C. Jin, B. Sendhoff, “Optimization of micro heat exchanger: CFD, analytical approach and multi-objective evolutionary algorithms,” in *Int. J. Heat Mass Transf.*, vol. 49, no. 5–6, pp. 1090-1099, Mar. 2006.
- [81] C. Leng, X.D. Wang, T.H. Wang, W.M. Yan, “Multi-parameter optimization of flow and heat transfer for a novel double-layered microchannel heat sink,” in *Int. J. Heat Mass Transf.*, vol. 84, pp. 359-369, May. 2015.
- [82] T.H. Wang, H.C. Wu, J.H. Meng, W.M. Yan, “Optimization of a double-layered microchannel heat sink with semi-porous-ribs by multi-objective genetic algorithm,” in *Int. J. Heat Mass Transf.*, vol. 149, p. 119217, Mar. 2020.
- [83] M. Yang, B.Y. Cao, “Multi-objective optimization of a hybrid microchannel heat sink combining manifold concept with secondary channels,” in *Appl. Therm. Eng.*, vol. 181, no. 25, p. 115592, Nov. 2020.
- [84] J. He, L. Shi, H. Tian, X. Wang, X. Sun, M. Zhang, Y. Yao, G. Shu, “Applying artificial neural network to approximate and predict the transient dynamic behavior of CO<sub>2</sub> combined cooling and power cycle,” in *Energy*, vol. 285, no. 15, p. 129451 Dec. 2023.
- [85] I.K. Kang, T.Y. Shin, J.H. Kim, “Observation-informed modeling of artificial neural networks to predict flow and bleeding of cement-based materials,” in *Constr. Build. Mater.*, vol. 409, no. 15, p. 133811, Dec. 2023.
- [86] A. Sikirica, L. Grbčić, L. Kranjčević, “Machine learning based surrogate models for microchannel heat sink optimization,” in *Appl. Therm. Eng.*, vol. 222, no. 5, p. 119917, Mar. 2023.
- [87] H.N. Khaboshan, F. Jaliliantabar, A.A. Abdullah, S. Panchal, A. Azarinia, “Parametric investigation of battery thermal management system with phase change material, metal foam, and fins; utilizing CFD and ANN models,” in *Appl. Therm. Eng.*, vol. 247, no. 15, p. 123080, June 2024.

- [88] S. Kumar, S.V.S.S.N.V.G. K. Murthy, B.V.R. Kumar, D. Parmar, “Multi-physics study on double-diffusion convective flow in an inverted T-shaped porous enclosure: ANN-based parametric estimation,” in *Phys. Lett. A*, vol. 518, no. 5, p. 129681, Sept. 2024.
- [89] A. Raj, S.K. Sharma, “Device parameter prediction for GAA junctionless nanowire FET using ANN approach,” in *Microelectron. J.*, vol. 147, p. 106192, May 2024.
- [90] B.A. Almahmmadi, H.A. Refaey, M.T. Abdelghany, S. Bendoukha, M. Mansour, M.A. Sharafeldin, “Thermo-fluid performance for helical coils inserted in a tube using hybrid CFD-ANN approach,” in *Therm. Sci. Eng. Prog.*, vol. 51, p. 102661, June 2024.
- [91] Z.Z. Li, Z.F. Feng, Q.Y. Zhang, J.Y. Zhou, J.X. Zhang, F.W. Guo, “Thermal-hydraulic performance and multi-objective optimization using ANN and GA in microchannels with double delta-winglet vortex generators,” in *Int. J. Therm. Sci.*, vol. 193 p. 108489, Nov. 2023.
- [92] D.D. Ma, G.D. Xia, Y.T. Jia, Y.F. Li, J. Wang, “Multi-parameter optimization for micro-channel heat sink under different constraint conditions,” in *Appl. Therm. Eng.*, vol. 120, no. 25, pp. 247-256, June 2017.
- [93] M.E. Polat, S. Cadirci, “Artificial neural network model and multi-objective optimization of microchannel heat sinks with diamond-shaped pin fins,” in *Int. J. Heat Mass Transf.*, vol. 194, no. 15, p. 123015, Sept. 2022.
- [94] S. Sabzpoushan, M. Sabouri, “Secondary flow through lateral passages to improve hydrothermal performance of liquid-cooled microchannel heat sinks,” in *Appl. Therm. Eng.*, vol. 227, no.5, p. 120009, June 2023.
- [95] Y.K. Wang, J.Z. Liu, K.M. Yang, J.Y. Liu, X.H. Wu, “Performance and parameter optimization design of microchannel heat sink with different cavity and rib combinations,” in *Case Stud. Therm. Eng.*, vol. 53, p. 103843, Jan. 2024.
- [96] X. Chen, R. Tu, X. Yang, “Parameter prediction optimization of data center’s heat dissipation system using machine learning algorithms,” in *Appl. Therm. Eng.*, vol. 232, p. 121047, Sept. 2023.

- [97] Q.R. Adebowale, "Effect of training algorithms and network architecture on the performance of multi-band ANN-Based path loss prediction model," in *Proc. 2022 IEEE Nigeria 4th International Conference on Disruptive Technologies for Sustainable Development (NIGERCON)*, Lagos, Nigeria, 2022, pp. 1-5.
- [98] A. Oulmelk, M. Sрати, L. Afraites, A. Hadri, "An artificial neural network approach to identify the parameter in a nonlinear subdiffusion model," in *Commun. Nonlinear Sci. Numer. Simul.*, vol. 125, p. 107413, Oct. 2023.
- [99] E. Bas, E. Egrioglu, T. Cansu, "Robust training of median dendritic artificial neural networks for time series forecasting," in *Expert Syst. Appl.*, vol. 238, Part. C, no. 15, p. 122080, Mar. 2024.
- [100] A. Swietlicka, K. Kolanowski, "Homogeneous ensemble model built from artificial neural networks for fault detection in navigation systems," in *J. Comput. Appl. Math.*, vol. 432, p. 115279, Nov. 2023.
- [101] A. Blum and T. Mitchell, "Combining labeled and unlabeled data with co-training," in *Proc. the eleventh annual conference on Computational learning theory*, New York, NY, USA: ACM, Jul. 1998, pp. 92–100.
- [102] S. Chen, J. Chen, T. Zhang and S. Wei, "Semi-supervised learning based on hybrid neural network for the signal integrity analysis," in *IEEE Trans. Circuits Syst. II, Exp. Briefs.*, vol. 67, no. 10, pp. 1934-1938, Oct. 2020.
- [103] C. Feng, P. Zhang, D. Wang, W. Zhao, J. Wang, P. Christodoulides, "Hybrid neural network based multi-objective optimal design of hybrid pin-fin microchannel heatsink for integrated microsystems," in *Int. C. Heat Mass Transf.*, vol. 159, Part B, p. 108137, Dec. 2024.
- [104] D. Wang et al., "Convolutional Neural Network-Based Deep Learning for Intelligent OSNR Estimation on Eye Diagrams," in *Proc. 2017 European Conference on Optical Communication (ECOC)*, Gothenburg, Sweden, 2017, pp. 1-3.
- [105] X.J. Wei, Y. Joshi, M.K. Patterson, "Experimental and numerical study of a stacked microchannel heat sink for liquid cooling of microelectronic devices," in *J. Heat Transf.*, vol. 129, no. 10, pp. 1432–1444, Oct. 2007.

- [106] W. Qu, I. Mudawar, “Experimental and numerical study of pressure drop and heat transfer in a single-phase micro-channel heat sink,” in *Int. J. Heat Mass Transf.*, vol. 45, no. 12, pp. 2549–2565, June 2002.